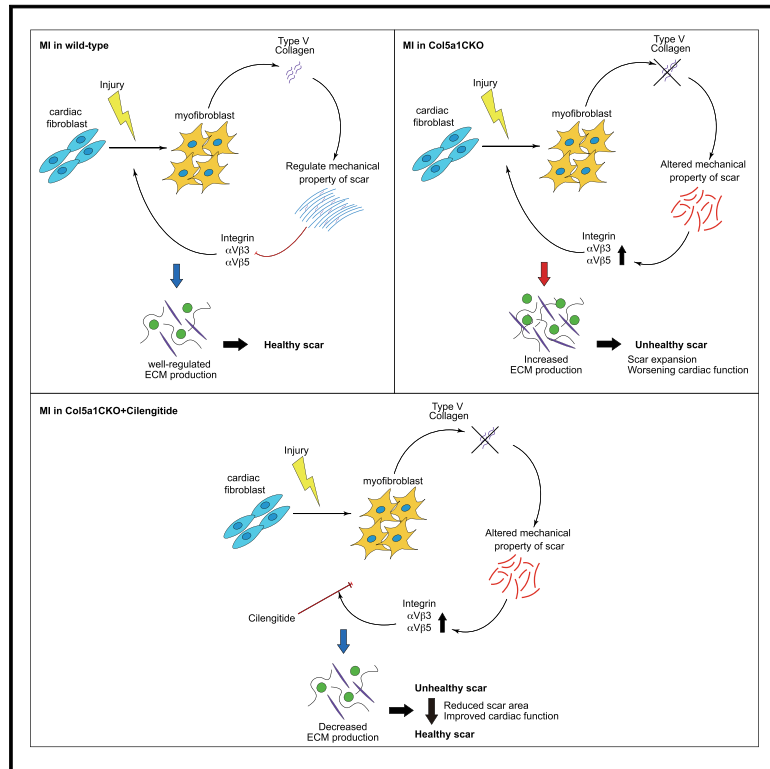


# Type V Collagen in Scar Tissue Regulates the Size of Scar after Heart Injury

## Graphical Abstract



## Authors

Tomohiro Yokota, Jackie McCourt, Feiyang Ma, ..., Marcus Seldin, Aldons J. Lusic, Arjun Deb

## Correspondence

adeb@mednet.ucla.edu

## In Brief

Scar tissue size following heart injury is a predictor of cardiovascular outcomes. Yokota et al. find that a specific collagen, type V, plays a paradoxical role in limiting scar size by altering the mechanical properties of developing scar tissue.

## Highlights

- Collagen V deficiency increases scar size after acute heart injury
- Mechanical properties of scars are altered with Col V deficiency
- Altered mechanosensitive cues augment myofibroblast formation in scar
- Inhibition of specific integrins rescues increased scarring in Col-V-deficient states



## Article

# Type V Collagen in Scar Tissue Regulates the Size of Scar after Heart Injury

Tomohiro Yokota,<sup>1,2,3,4,5,6</sup> Jackie McCourt,<sup>7</sup> Feiyang Ma,<sup>3,4,5</sup> Shuxun Ren,<sup>5,8</sup> Shen Li,<sup>1,2,3,4,5,6</sup> Tae-Hyung Kim,<sup>7</sup> Yerbol Z. Kurmangaliyev,<sup>9</sup> Rohollah Nasiri,<sup>6,10,11</sup> Samad Ahadian,<sup>6,10,12</sup> Thang Nguyen,<sup>10</sup> Xing Haw Marvin Tan,<sup>6,10,15</sup> Yonggang Zhou,<sup>1,2,3,4,5,6</sup> Rimao Wu,<sup>1,2,3,4,5,6</sup> Abraham Rodriguez,<sup>1,2,3,4,5,6</sup> Whitaker Cohn,<sup>16</sup> Yibin Wang,<sup>5,8</sup> Julian Whitelegge,<sup>16</sup> Sergey Ryazantsev,<sup>6</sup> Ali Khademhosseini,<sup>6,10,12,13,14</sup> Michael A. Teitell,<sup>10,18</sup> Pei-Yu Chiou,<sup>6,10,15</sup> David E. Birk,<sup>19</sup> Amy C. Rowat,<sup>7,10</sup> Rachele H. Crosbie,<sup>4,5,7</sup> Matteo Pellegrini,<sup>3,4,5</sup> Marcus Seldin,<sup>17</sup> Aldons J. Lusic,<sup>1,20</sup> and Arjun Deb<sup>1,2,3,4,5,6,21,\*</sup>

<sup>1</sup>Division of Cardiology, Department of Medicine, David Geffen School of Medicine, University of California, Los Angeles, CA 90095, USA

<sup>2</sup>UCLA Cardiovascular Theme, David Geffen School of Medicine, University of California, Los Angeles, CA 90095, USA

<sup>3</sup>Department of Molecular, Cell and Developmental Biology, College of Letters and Sciences, University of California, Los Angeles, CA 90095, USA

<sup>4</sup>Eli & Edythe Broad Center of Regenerative Medicine and Stem Cell Research, University of California, Los Angeles, CA 90095, USA

<sup>5</sup>Molecular Biology Institute, University of California, Los Angeles, CA 90095, USA

<sup>6</sup>California Nanosystems Institute, University of California, Los Angeles, CA 90095, USA

<sup>7</sup>Department of Integrative Biology and Physiology, University of California, CA 90095, USA

<sup>8</sup>Department of Anesthesiology, David Geffen School of Medicine, University of California, Los Angeles, CA 90095, USA

<sup>9</sup>Department of Biological Chemistry, David Geffen School of Medicine, Los Angeles, CA 90095, USA

<sup>10</sup>Department of Bioengineering, School of Engineering, University of California, Los Angeles, CA 90095, USA

<sup>11</sup>Department of Mechanical Engineering, Sharif University of Technology, Tehran 11365-11155, Iran

<sup>12</sup>Terasaki Institute for Biomedical Innovation (TIBI), Los Angeles, CA 90024, USA

<sup>13</sup>Department of Chemical Engineering, School of Engineering, University of California, Los Angeles, CA 90095, USA

<sup>14</sup>Department of Radiology, David Geffen School of Medicine, University of California, Los Angeles, CA 90095, USA

<sup>15</sup>Department of Mechanical and Aerospace Engineering, University of California, Los Angeles, CA 90095, USA

<sup>16</sup>Passarow Mass Spectrometry Laboratory, Semel Institute for Neuroscience and Behaviour, David Geffen School of Medicine, Los Angeles, CA 90095, USA

<sup>17</sup>Department of Biological Chemistry and Center for Epigenetics and Metabolism, University of California, Irvine, CA 92697, USA

<sup>18</sup>Department of Pathology and Laboratory Medicine, University of California, Los Angeles, CA 90095, USA

<sup>19</sup>University of South Florida College of Medicine, Tampa, FL 33612, USA

<sup>20</sup>Department of Genetics, David Geffen School of Medicine, Los Angeles, CA 90095, USA

<sup>21</sup>Lead Contact

\*Correspondence: [adeb@mednet.ucla.edu](mailto:adeb@mednet.ucla.edu)

<https://doi.org/10.1016/j.cell.2020.06.030>

## SUMMARY

Scar tissue size following myocardial infarction is an independent predictor of cardiovascular outcomes, yet little is known about factors regulating scar size. We demonstrate that collagen V, a minor constituent of heart scars, regulates the size of heart scars after ischemic injury. Depletion of collagen V led to a paradoxical increase in post-infarction scar size with worsening of heart function. A systems genetics approach across 100 in-bred strains of mice demonstrated that collagen V is a critical driver of postinjury heart function. We show that collagen V deficiency alters the mechanical properties of scar tissue, and altered reciprocal feedback between matrix and cells induces expression of mechanosensitive integrins that drive fibroblast activation and increase scar size. Cilengitide, an inhibitor of specific integrins, rescues the phenotype of increased post-injury scarring in collagen-V-deficient mice. These observations demonstrate that collagen V regulates scar size in an integrin-dependent manner.

## INTRODUCTION

Following acute myocardial infarction (MI), dead cardiac muscle is replaced by scar tissue. Clinical studies demonstrate that scar size in patients with prior MI is an independent predictor of mortality and outcomes, even when normalized with respect to car-

diac function (Gulati et al., 2013). Despite the immense pathophysiologic importance of scar burden, little is known about factors that regulate scar size after ischemic cardiac injury (Frangogiannis, 2017).

To identify factors determining scar size after MI, we subjected animals to ischemic cardiac injury and performed transcriptional



profiling of heart scars isolated from 3 days to 6 weeks post injury. We observed that scars rapidly attained transcriptional maturity, and there were minimal transcriptional changes in the maturing scar tissue beyond 2 weeks of injury. We thus hypothesized that genes that regulate scar size are likely to be differentially expressed early after ischemic injury. Collagens were one of the most highly differentially upregulated genes in the injured heart early after ischemic cardiac injury. Collagens I and III are the most abundant collagens present in the uninjured heart, comprising approximately 90%–95% of all cardiac collagens (Bashey et al., 1992; Frangogiannis, 2017; Weber, 1989). They belong to the family of fibrillar collagens that are thought to confer mechanical strength to the cardiac matrix. However, more than 26 different types of collagens have been described in mammals, and we observed a large number of collagens that are minimally expressed in the uninjured heart to be robustly induced following injury. The physiological necessity for the heterogeneity of collagen expression in scar tissue is unclear.

In this report, we demonstrate that collagen V (Col V), a fibrillar collagen that is minimally expressed in the uninjured heart and a minor component of scar tissue, limits scar size after ischemic cardiac injury. Animals lacking Col V in scar tissue exhibit a significant and paradoxical increase in scar size after ischemic injury. In the absence of Col V, scars exhibit altered mechanical properties that drive integrin-dependent mechanosensitive feedback on fibroblasts, augmenting fibroblast activation, extracellular matrix (ECM) secretion, and increase in scar size. Modulation of such mechanosensitive feedback cues rescues the Col-V-deficient phenotype of increased scarring. These findings provide insight into the physiological role of Col V in regulating scar size and have implications for the treatment of dysregulated wound healing in genetic diseases caused by mutations in Col-V-encoding genes.

## RESULTS

### Heart Scars Attain Transcriptional Maturity Early after Acute Ischemic Cardiac Injury

We subjected adult C57BL/6 mice to ischemic cardiac injury (Ubil et al., 2014) by permanent ligation of the left anterior descending coronary artery and observed acute and progressive loss of cardiac function (Figure S1A). Hearts were harvested at 3, 7, 14, 21, and 42 days after ischemic injury, and the fibrotic scar tissue in the injured and the region remote to the area of injury were dissected from the same heart for RNA sequencing (RNA-seq) to quantify temporal changes in gene expression. Principal-component analysis (PCA) showed samples from remote regions at all time points clustered together (Figure 1A). Principal component 1 (PC1) separated transcriptional signatures of injured and uninjured regions across all time points examined (Figure 1A), suggesting that gene expression differences continue to persist between the injured and uninjured regions. PC2 separated the samples of scar tissue in a temporal manner following injury (Figure 1A). In particular, significant differences were observed between scar tissue harvested at 3 and 7 days following injury, as well as between that harvested at 7 days and subsequent time points. However, the transcriptional signatures of the injured region of the hearts at 14, 21,

and 42 days after injury clustered together, demonstrating that most transcriptional changes occur within 2 weeks of injury (Figure 1A). Analysis of differentially expressed genes (DEGs) demonstrated that the largest number of DEGs occurred between injured and uninjured samples at each analyzed time point (from 1,210 to 1,931) (Figure 1B; Table S1). Comparisons between time points of injured regions detected 247 and 100 DEGs between days 3 and 7, and days 7 and 14, respectively. Almost no differences were detected between scar tissue harvested at later time points (Figure 1B). These data demonstrate that major transcriptional changes within scar tissue occur early after injury and further maturation of scar tissue beyond 2 weeks is not associated with significant transcriptional changes.

We hypothesized that genes that directly regulate scar size are upregulated early after ischemic cardiac injury. Collagens were one of the most differentially upregulated genes in the injured region early after injury. We examined expression patterns of genes encoding obligatory subunits of all types of collagen (Figure 1C). In addition to type I and III collagens, we observed genes encoding for various subunits of Col V, VI, VIII, XI, XII, XIV, XV, XVI, and XVIII to be significantly induced after heart injury (Figure 1C) with expression of most collagens increasing by 3 days, peaking at 7 days, and declining by 42 days after injury (Figure 1C). Next, to confirm our findings, we performed qPCR for the principal genes encoding all mammalian collagens (Figure 1D, Figure S1B). *Col1a1* and *Col3a1* demonstrated the most robust gene expression changes after acute injury, consistent with them being the principal cardiac collagens (Figure 1D). Collagen-encoding genes that are known to be abundantly expressed in extra-cardiac tissues such as *Col2a1*, *Col7a1*, and *Col9a2* demonstrated dynamic expression changes (Figure S1B), but absolute levels of expression were low (Figure S1C). Taken together, these data demonstrate that a diverse set of collagen genes, including several that are minimally expressed in the uninjured heart, are robustly induced early after acute ischemic cardiac injury.

### *Col5a1* Expression Overlaps *Col1a1* and *Col3a1* Expression in the Infarcted Region with a Single Cardiac Fibroblast Expressing All Three Collagens

We next dissected the nascent scar tissue at 7 days following injury and first performed proteomic analysis of the collagens differentially expressed between the scar and uninjured tissue (Figure 2A). We confirmed increased levels of the fibrillar collagen peptide chains COL1A1, COL3A1, and COL5A1 and other collagen peptides (Figure 2A). *Col1a1* and *Col3a1* genes were the most abundantly expressed fibrillar collagen genes in scar tissue at 7 days following injury (Figure 2B). Out of other fibrillar collagens (I, V, XI), *Col5a1* was the only one that was induced robustly early in scar tissue (Figure 2B).

We next examined the spatial expression of the fibrillar collagens Col I, III, and V. The objective of this experiment was to determine whether the same cell expressed all three fibrillar collagens (I, III, and V) or whether the collagens were expressed by different cells in scar tissue. To prevent cross reactivity of antibodies to different collagens and to facilitate accurate fluorophore colocalization, we chose to perform RNA fluorescence *in situ* hybridization (RNA-FISH) to determine the spatial

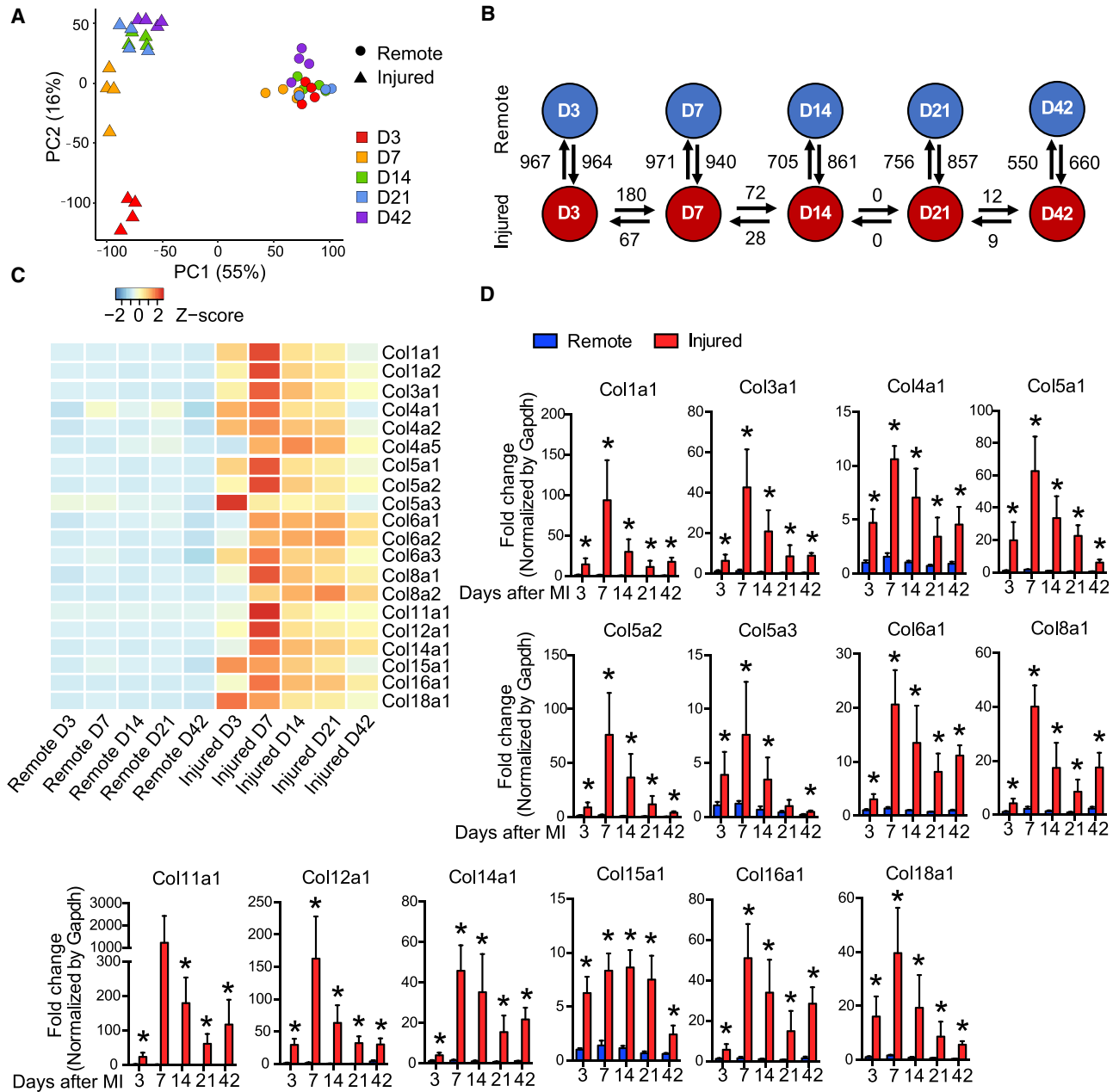


**Figure 1. Temporal Changes in Gene Expression of Scar Tissue following Acute Ischemic Cardiac Injury**

(A) Principal-component analysis based on expression profiles of all genes (n = 4).

(B) Summary of differential gene expression analysis. Arrows and numbers indicate direction and numbers of differentially expressed genes detected in each pairwise comparison (false discovery rate [FDR] 1%, fold change > 4).

(C) Heatmap with expression patterns of collagen genes (n = 4).

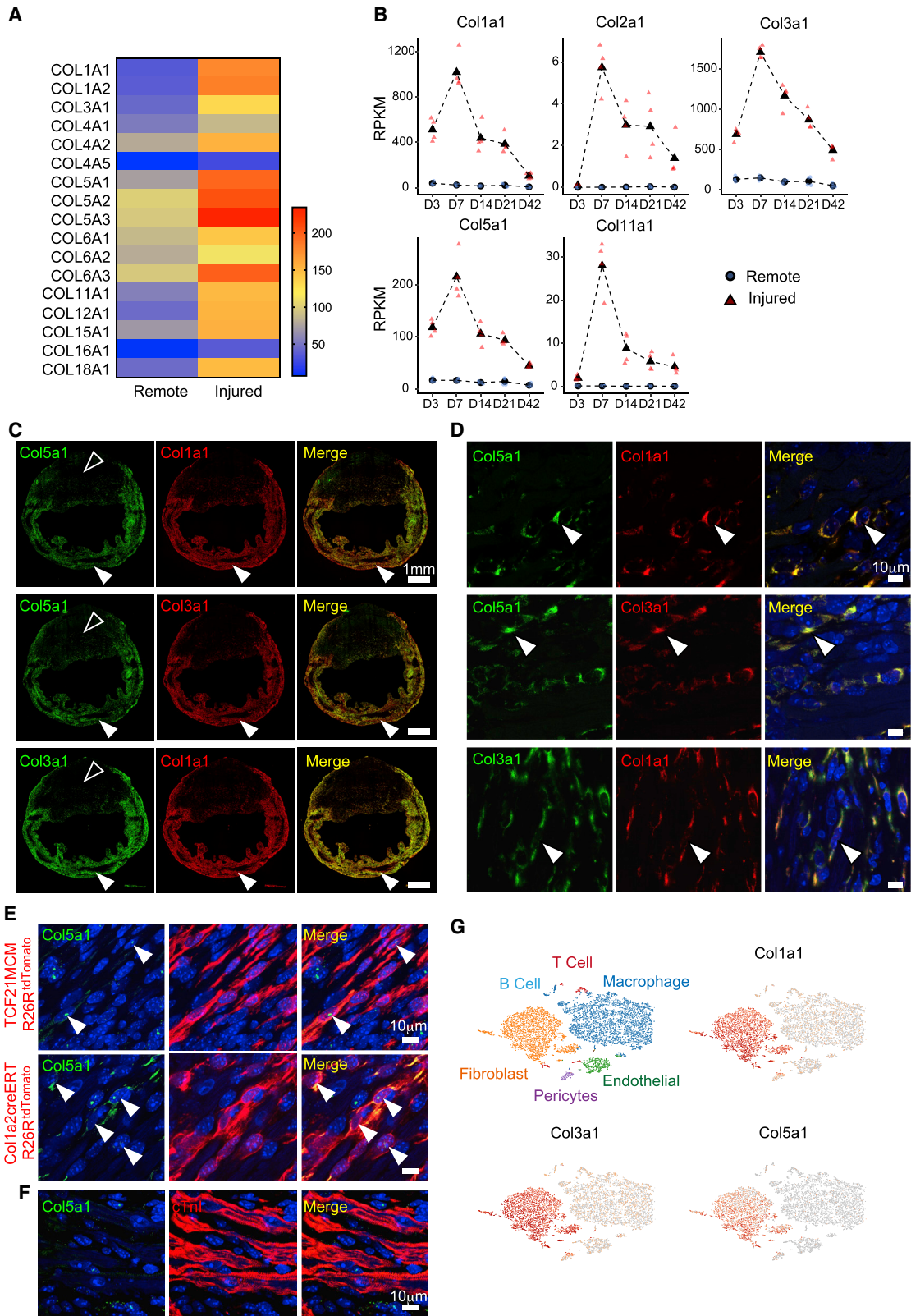
(D) Expression of collagen genes encoding for obligatory units of the respective collagen by qPCR (mean ± SD, \*p < 0.05, n = 5).

See also [Figure S1](#).

expression of *Col5a1* versus *Col1a1* or *Col3a1* post injury. RNA-FISH demonstrated robust and overlapping expression of *Col5a1* with either *Col3a1* or *Col1a1* mRNA in the injured region of the heart ([Figure 2C](#)), and we observed the same cell to express both *Col5a1* and *Col3a1/Col1a1* ([Figure 2D](#)). To confirm these observations, we performed RNA-FISH in mice

with genetically labeled cardiac fibroblasts. For this purpose, mice expressing fibroblast Cre drivers (*Col1a2CreERT* or *TCF21MerCreMer*) were crossed with the lineage reporter *Rosa26tdTomato* mice ([Acharya et al., 2011](#); [Pillai et al., 2017](#); [Zheng et al., 2002](#)) and tamoxifen was administered to induce genetic labeling of cardiac fibroblasts ([Pillai et al., 2017](#); [Ubil](#)





(legend on next page)

et al., 2014). RNA-FISH on hearts harvested at 7 days post injury demonstrated tdTomato-labeled cardiac fibroblasts to express *Col5a1* (Figure 2E). As cardiomyocytes are known to express collagens (Heras-Bautista et al., 2019), we performed immunostaining for cardiac troponin I, but did not observe cardiomyocytes to express *Col5a1* (Figure 2F). To provide corroborative evidence, we next performed single-cell RNA-seq (scRNA-seq) of the non-myocyte cell fraction of the injured region of the heart at 7 days post injury and observed significant overlap between *Col5a1* expression and *Col3a1* and *Col1a1* expression (Figure 2G). Taken together, these observations demonstrate that Col I, III, and V have overlapping expression in the area of injury and that a single cardiac fibroblast has the ability to produce both Col V and Col I/III.

### Mice Deficient in Type V Collagen Exhibit a Paradoxical Increase in Fibrosis and Scar Size after Heart Injury

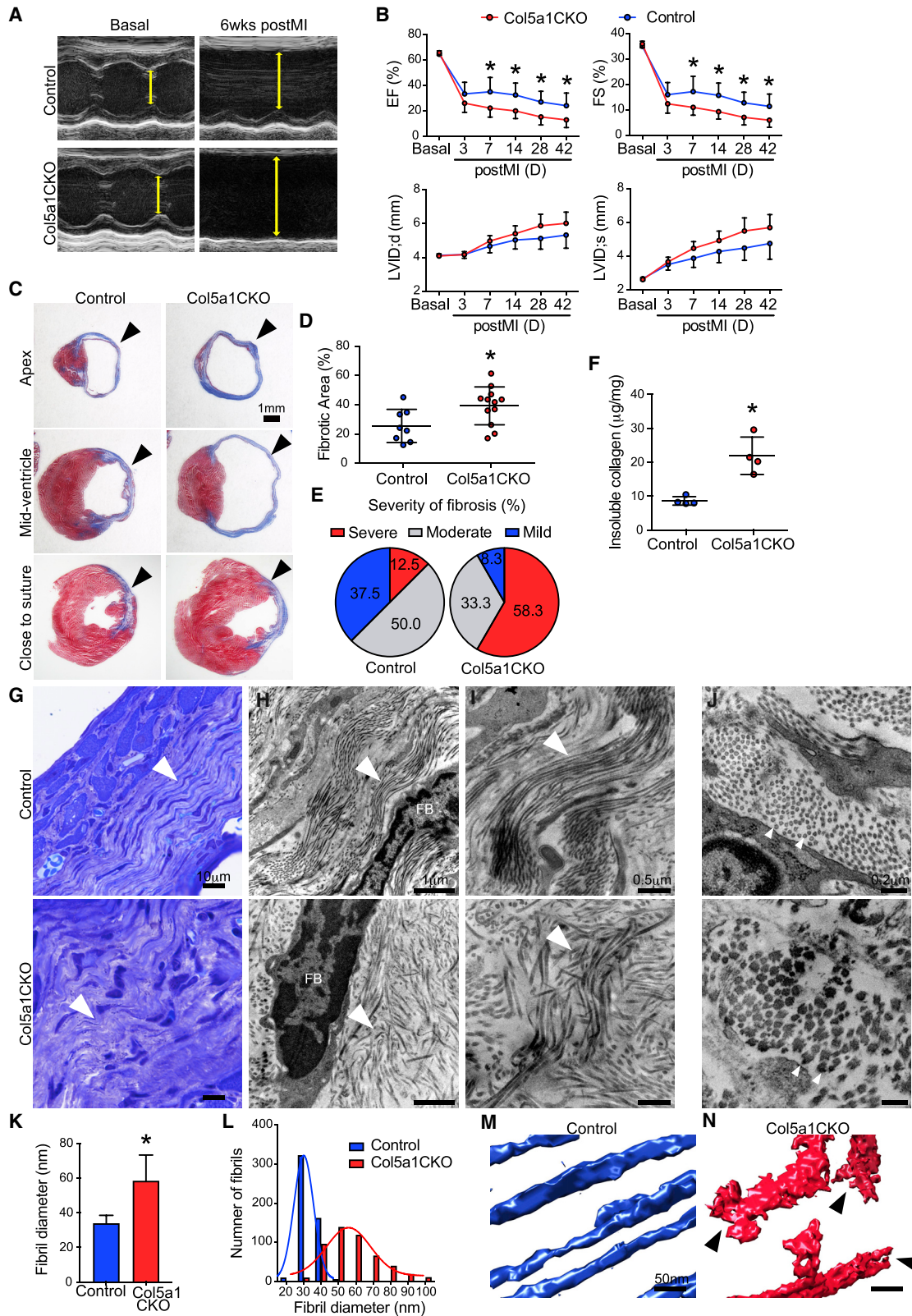
Homozygous deletion of the *Col5a1* gene results in absence of functional Col V protein in tissues and causes early embryonic lethality (Wenstrup et al., 2004). Mice heterozygous for *Col5a1* deficiency exhibit increased fibrosis in their valves and myocardium at birth, suggestive of a role of Col V in regulating ECM output (Lincoln et al., 2006). To determine the functional role of Col V in the injured heart, we first crossed the *Col1a2CreERT* mice with *Col5a1* floxed mice (Sun et al., 2011). We administered tamoxifen to progeny mice for 5 days prior to injury and continued for seven days post injury to maximize labeling and generate *Col5a1*CKO (conditional knockout) mice. Control animals included littermates that lacked the Cre transgene but had both *Col5a1* alleles floxed and were injected with tamoxifen in an identical manner. RNA-FISH on the *Col5a1*CKO hearts demonstrated 66.6% ± 17.8% reduction of *Col5a1* expression (mean ± SD, \**p* < 0.05) (Figures S2A and S2B). We observed significant depression of cardiac contractile performance (ejection fraction [EF] and fractional shortening [FS]) by 7 days in the *Col5a1*CKO group following ischemic injury, which persisted throughout the next 6 weeks (mean ± SD, \**p* < 0.05) (Figures 3A and 3B), and this was associated with a strong trend toward chamber dilatation (*p* = 0.06 for LVID(d) at 6 weeks post MI) (Figure 3B). Histology demonstrated that the area of fibrotic scar tissue was significantly greater by 1.5-fold in the *Col5a1*CKO compared to wild-type littermates (mean ± SD, \**p* < 0.05) (Figures 3C and 3D). To further analyze the wound healing response in *Col5a1*CKO animals, we determined the fraction of animals that exhibited mild, moderate, or severe fibrosis after ischemic injury. We defined mild, moderate,

and severe fibrosis as scar surface area less than 20%, between 20% and 40%, and greater than 40% of the left ventricular surface area, respectively, measured at 6 weeks following injury, and observed that greater than 58% of the *Col5a1*CKO animals had severe fibrosis compared to approximately 12% of animals in control littermates (Figure 3E). There were no significant differences in interstitial fibrosis of the uninjured myocardium in *Col5a1*CKO and control mice (Figure S2C). As scars mature, collagen fibrils undergo crosslinking within scar tissue and become less soluble. We found that the amount of insoluble collagen (surrogate for crosslinked collagen) was increased by 254% ± 64% (mean ± SD, \**p* < 0.05) in the *Col5a1*CKO group at 6 weeks post injury (Figure 3F). Col V is thought to initiate organization of Col I and III fibrils in the ECM and is intercalated between the staggered arrangement of Col I and III fibrils maintaining organization of the ECM (Wenstrup et al., 2004). We performed toluidine blue staining and observed the typical wavy nature of collagen fibrils compactly arranged in parallel in the injured control animal hearts, but the hearts from the *Col5a1*CKO animals showed a loose arrangement of collagen fibers (Figure 3G). We performed transmission electron microscopy, and instead of the smooth parallel arrangement of collagen fibrils in scars of control animals, we observed fibrillar disarray with fibrils running at orthogonal axes to each other in the *Col5a1*CKO scars (Figures 3H and 3I). Collagen fibril diameters were significantly greater (Figures 3J and 3K), and a histogram of the numbers of collagen fibrils versus their diameter demonstrated a rightward shift of the curve in *Col5a1*CKO mice (Figure 3L). Finally, we performed electron tomography and observed shorter length, irregular fibrillar structure and breaks in collagen fibrils in the *Col5a1*CKO scar compared to wild-type scar (Figures 3M and 3N). Taken together, these observations demonstrate that deletion of type V collagen leads not only to increased scar size, but also results in grossly abnormal scar architecture.

As increased scar size in the post-infarcted heart is associated with adverse phenotypes such as hypertrophy of cardiomyocytes in the border zone (Frangogiannis, 2017, 2019), we harvested hearts at 6 weeks following injury and observed significantly greater heart-weight/body-weight ratios of *Col5a1*CKO hearts compared to control littermates (mean ± SD, \**p* < 0.05) with no significant differences in body weight alone (Figures S2D and S2E). Immunostaining for cardiac troponin I confirmed robust hypertrophy of cardiomyocytes abutting the margins of the scar (border zone) in *Col5a1*CKO animals (Figures S2F and S2G).

### Figure 2. Expression of *Col5a1* in Relation to *Col1a1* and *Col3a1*

- (A) Proteomic analysis of individual collagen chains in injured and remote region of myocardium at 7 days post MI (*n* = 3).  
(B) Normalized expression levels (reads per kilobase of transcript, per million mapped reads [RPKM]) for selected collagen genes. Average expression levels across time points are shown in black symbols and dashed lines. Expression levels for individual replicates are shown in colored symbols (*n* = 4).  
(C) RNA-FISH to demonstrate expression of *Col5a1*, *Col1a1*, and *Col3a1* in the heart at 7 days post MI (solid arrowhead, representative images, *n* = 4, unfilled arrowhead indicates remote region, images were acquired and stitched together using Nikon software).  
(D) Higher magnification demonstrating co-localization of *Col5a1* with *Col1a1* and *Col3a1* within the same cell (arrows, representative images, *n* = 4).  
(E and F) Expression of *Col5a1* in cardiac fibroblasts genetically labeled by the TCF21 or *Col1a2* label (E) but not in cardiomyocytes (Troponin I stained) in the injury region (F) (arrows, representative images, *n* = 3).  
(G) Single cell RNA-seq of non-myocytes at 7 days post MI demonstrating typical cell phenotypes in clusters and distribution of *Col1a1*, *Col3a1*, and *Col5a1* (*n* = 3).



(legend on next page)



### Validation of Phenotype of Collagen V Deficiency in the Injured Heart Using an Alternative Cre Driver

To validate our observations noted with the Col1a2Cre driver, we generated another CKO of the *Col5a1* gene using the Tcf21Mer-CreMer driver (Tcf21MCM), Tcf21 being a specific marker of cardiac fibroblasts in the adult heart (Acharya et al., 2011; Kanisicak et al., 2016). The Tcf21MCM mice were crossed with the Col5a1 floxed mice and tamoxifen-administered 5 days prior to injury and for 7 days following injury to create Tcf21MCM:Col5a1CKO mice. Controls included littermate animals that had both *Col5a1* alleles floxed but lacked the Cre transgene and were injected with tamoxifen in an identical manner. At 7 days post injury, *Col5a1* expression in the injury region of Tcf21MCM:Col5a1CKO decreased by almost  $60.1\% \pm 10.1\%$  (mean  $\pm$  SD,  $*p < 0.05$ ) (Figures S3A and S3B). Tcf21MCM:Col5a1CKO mice exhibited significant decline in cardiac contractile function by 7 days of injury that persisted for the next 6 weeks (Figures S3C and S3D), and this was also associated with a trend toward greater chamber size (LVID) (Figure S3D). We observed a significant 1.5-fold increase in scar size in Tcf21MCM:Col5a1CKO animals versus control littermates (mean  $\pm$  SD,  $*p < 0.05$ ) (Figures S3E and S3F). The fraction of animals that exhibited severe fibrosis (>40% surface area) was 40% in the Tcf21MCM:Col5a1CKO animals compared to approximately 11% in the control littermates (Figure S3G). The Tcf21MCM:Col5a1CKO animals exhibited significantly greater heart-weight/body-weight ratios at 6 weeks after injury (no change in body weight) (Figures S3H and S3I), and histology confirmed significantly greater myocyte hypertrophy (mean  $\pm$  SD,  $*p < 0.05$ ) (Figures S3J and S3K). To exclude a potential role of tamoxifen in contributing to post-injury contractile dysfunction, tamoxifen was administered in an identical manner to TCF21MCM mice but without the Col5a1 floxed alleles. No differences in cardiac function were observed within 1 and 2 weeks of injury following tamoxifen administration (Figure S4A). Taken together, these observations using an independent Cre driver mirror and provide compelling evidence that deletion of type V collagen leads to an exacerbated fibrotic repair response.

To complement these observations, we subjected the Col5a1 heterozygous KO mice (Col5a1<sup>+/-</sup>) (Wenstrup et al., 2004) to ischemic cardiac injury. Compared to wild-type littermates, the heterozygote Col5a1KO exhibited a significant reduction in car-

diac contractile function by 1 and 2 weeks of injury and exhibited greater degree of cardiac hypertrophy as assessed by heart-weight/body-weight ratios (Figures S4B–S4D). The data presented earlier show that scars rapidly attain transcriptional maturity, and cardiac function is significantly compromised within 7 days of injury in the Col5a1CKO mice. Considering these observations, we postulated that the effects of Col5a1 deficiency on cardiac function early after cardiac injury may be related to its role in mediating an acute fibrotic repair response. To investigate this, we deleted Col5a1 after the acute phase of injury by administering tamoxifen from post-injury day 4 for 10 days. We observed that the TCF21MCM:Col5a1CKO animals (with deletion of Col5a1 after the acute injury response) did not exhibit a reduction in cardiac function at 2 weeks after injury (Figure S4E). These observations suggest that type V collagen affects post-injury cardiac function by playing a critical role in the early fibrotic repair response.

### Col5a1 Is a Critical Determinant of Post-Injury Heart Function vis-à-vis Other ECM Genes

A large number of collagens and other ECM proteins are upregulated in the region of scarring (in addition to Col V), and an argument can be made of the functional importance of Col V vis-à-vis other ECM proteins. We adopted a population genetics approach to determine the relative functional importance of Col V in driving post-injury cardiac function vis-à-vis other ECM genes. The hybrid mouse diversity panel (HMDP) comprises approximately 100 diverse inbred and recombinant strains of mice, and each strain can be subjected to an identical environmental perturbation to determine the genetic factors underlying responses (Ghazalpour et al., 2012; Lusi et al., 2016). The individual mouse strains in the HMDP were subjected to continuous isoproterenol infusion for 3 weeks that induces a chronic form of cardiac injury characterized by cardiomyocyte hypertrophy and interstitial fibrosis (Wang et al., 2016). Key traits of cardiac function such as cardiac contractility, chamber size, and fibrosis were followed over 3 weeks. Gene expression changes in the heart following isoproterenol infusion were determined in each strain, and these were statistically integrated with clinical traits to identify key loci or genes involved (Figure 4A) (Rau et al., 2017; Rau et al., 2015). We first analyzed a set of

### Figure 3. Animals with Col5a1 Deletion in Cardiac Fibroblasts Exhibit a Paradoxical Increase in Scar Tissue after Heart Injury

(A) M-mode echocardiogram demonstrating left ventricular (LV) walls and internal dimension (yellow line) prior to basal and 6 weeks post MI (representative images).

(B) Ejection fraction (EF), fractional shortening (FS), LV dimensions in end diastole (LVIDd), and end systole (LVIDs) at different time points post MI (n = 12/control and 27/CKO at basal, n = 10/control and 22/CKO at 3 days, n = 9/control and 15/CKO at 1 week, n = 9/control and 13/CKO at 2 weeks, n = 8/control and 12/CKO at 4 and 6 weeks post MI).

(C) Masson trichrome staining of hearts sectioned at the base (just distal to suture line) at mid-ventricle and apex 6 weeks post MI (representative images).

(D) Quantification of surface area of scar normalized to the surface area of the ventricle (n = 8/control and 12/CKO).

(E) Fraction of animals demonstrating mild/moderate or severe scarring at 6 weeks post MI.

(F) Measurement of insoluble collagen in scar tissue at 4 weeks post MI (n = 4)

(G) Toluidine blue staining of scar tissue at 4 weeks post MI (arrowhead, representative images, n = 2)

(H) Transmission electron microscopy (TEM) of scar area showing fibrillar disarray in the Col5a1CKO (arrowhead, FB = fibroblast)

(I) Higher magnification with TEM demonstrating fibrillar disarray with fibrils running in orthogonal axes to each other in the Col5a1CKO scar (arrowhead).

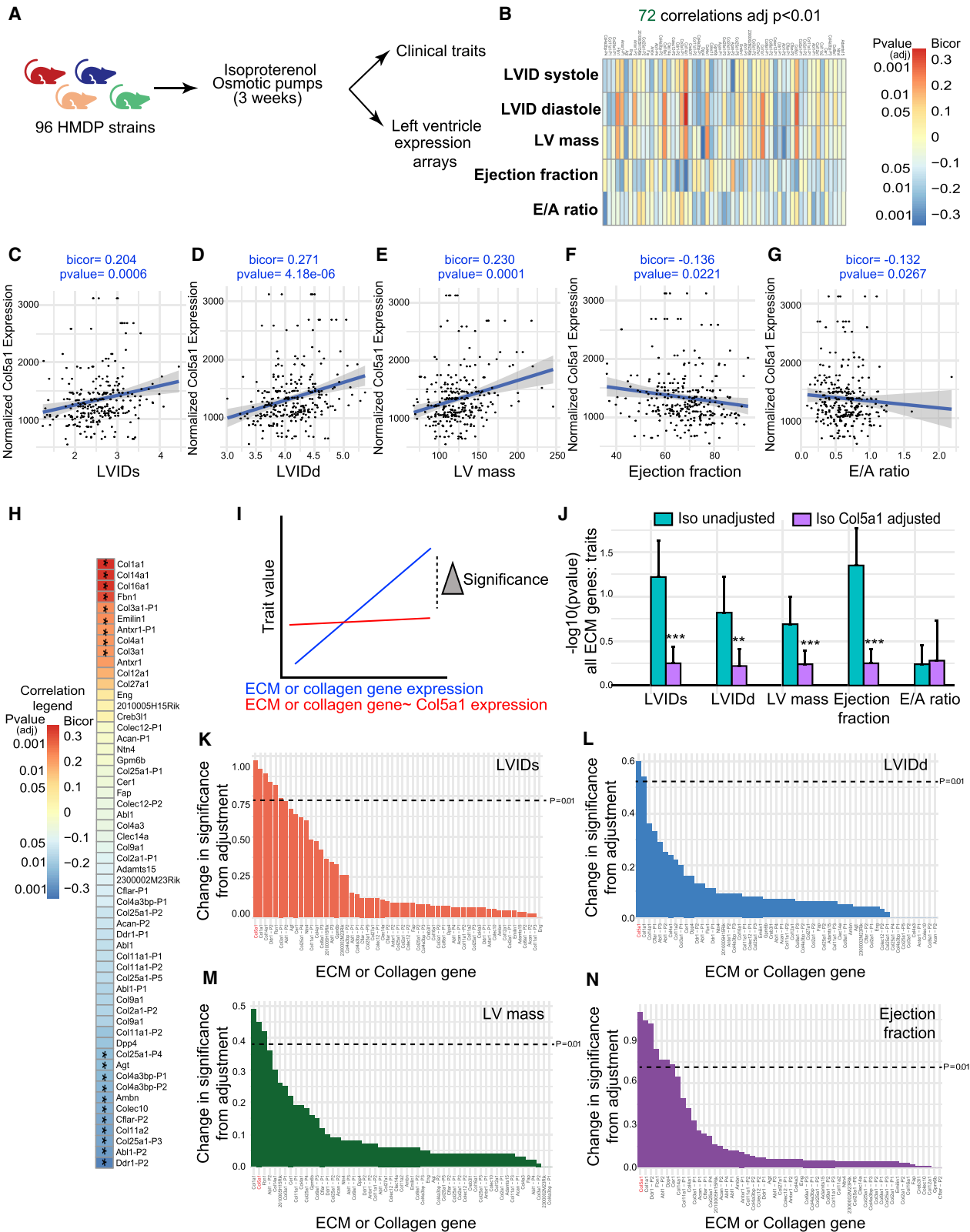
(J) Cross-sectional TEM view demonstrating fibril diameter size (arrowheads, n = 2 for all TEM).

(K) Average collagen fibril diameter in scars (n = 2).

(L) Histogram of collagen fibril diameters demonstrates a clear shift to the right in Col5a1CKO (n = 2).

(M and N) Electron tomogram of scar area from (M) control and (N) Col5a1CKO animal. Data shown as mean  $\pm$  SD,  $*p < 0.05$ .

See also Figures S2, S3, and S4.



(legend on next page)

ECM genes including collagens (Extracellular Matrix - GO:0031012 or Collagen Network - GO:0098645) that are abundantly expressed in the heart (Figure S4F) for correlations with clinical traits mentioned above (Figure 4B). *Col5a1* expression significantly correlated with cardiac traits of chamber size (LVID systole or diastole), cardiac hypertrophy (LV mass), and systolic and diastolic function (EF and E/A ratios) (Figures 4C–4G). We also observed genetic variation in the average expression of *Col5a1* across the strains in the HMDP (Figure S4G). We next analyzed the strength of association between *Col5a1* gene expression and the abovementioned set of ECM genes after isoproterenol. While several significant relationships were observed between *Col5a1* and ECM genes, there did not appear to be consistent patterns of overall positive or negative concordance (Figure 4H; Table S2). Given that (1) ECM genes strongly correlate with clinical traits and (2) *Col5a1* gene expression strongly correlates with a subset of ECM genes, we performed conditional analyses to evaluate the functional importance of *Col5a1* in mediating ECM:trait correlations. If *Col5a1* significantly contributed to the strength of correlation between ECM genes and traits, then adjustment for *Col5a1* expression should reduce the overall significance of correlations (Figure 4I). Conditioning on *Col5a1* expression led to a significant reduction in the overall strength of the association between rest of ECM genes and cardiac traits of chamber size, LV mass, and EF, while measures of diastolic compliance (E/A ratio) were not affected following *Col5a1* adjustment (Figure 4J). To test whether the correlation was specifically dependent on *Col5a1*, we conditioned on each of the other ECM genes and then assessed the change in significance of the correlations. As can be seen in Figures 4K–4N, while conditioning on several genes reduced the strength of the correlations, *Col5a1* showed the highest changes in significance following adjustment for LVID (systole), LVID (diastole), and ejection fraction. Only for cardiac mass was *Col5a1* in ranked second after *Col1a1* (Figure 4M). Using alternative cardiac injury models and complementary genetics approaches, these data support our principal observations of the physiological importance of Col V in regulating heart repair.

### Collagen V Deficiency Increases Myofibroblast Formation and Expression of Extracellular Matrix Genes in Scar Tissue

We next investigated mechanisms by which *Col5a1* deficiency leads to increase in scar size and examined whether the deficiency of *Col5a1* altered cell populations in the scar or affected

their transcriptional signatures. As maximal changes in transcriptional signatures of scars occur within the first few days after cardiac injury (Figure 1A), we harvested injured and uninjured regions of hearts, isolated non-myocyte cells, and subjected the cells to scRNA-seq using the 10x Genomics platform. A tSNE (t-distributed stochastic neighbor embedding) plot demonstrated the major cell populations in the injured region at 7 days (Figures 5A and S5A). We next determined the fraction of cells contributing to each cluster in the *Col5a1*CKO and wild-type controls (Figure 5B) and observed a comparable distribution of cells across fibroblast, endothelial, smooth muscle, and other cell populations with a slightly higher number of macrophages (Figures 5B and S5B). As *Col5a1* was deleted principally in cardiac fibroblasts, we focused on DEGs in the cardiac fibroblast cell cluster and first confirmed decreased expression of *Col5a1* in fibroblasts from *Col5a1*CKO mice (Figure 5C). We observed that fibroblasts from *Col5a1*CKO hearts exhibited significantly greater expression of *Acta 2* ( $\alpha$ smooth muscle actin or  $\alpha$ SMA) (Figure 5D), a gene that is not expressed by cardiac fibroblasts in the uninjured heart, but is a marker of myofibroblasts, a population of activated fibroblasts expressing smooth muscle contractile proteins (Frangogiannis, 2019). Myofibroblasts exhibit a synthetic and contractile phenotype and are thought to be the principal cells that secrete ECM proteins to form scar tissue (van den Borne et al., 2010). Other smooth-muscle-specific contractile proteins (*Cnn2* [calponin] and *Actn1* [Actinin 1]), markers of smooth muscle differentiation *SM22 $\alpha$*  (*Tagln*), proteins regulating smooth-muscle contraction such as regulatory myosins (*Myl 6* and *Myl9*), or calcium handling during smooth muscle contraction (*S100a4* and *s100a6*) were also significantly upregulated in fibroblasts of *Col5a1*CKO animals, suggestive of broad cytoskeletal organization and activation of fibroblasts (Figures 5E and S5C). Lysyl oxidase (*Lox*), which mediates crosslinking of collagen, was also upregulated (Figure S5C), consistent with increased amounts of insoluble collagen in scar tissue of *Col5a1*CKO hearts. We next examined the subsets of fibroblasts residing within the fibroblast cluster (Figure 5F) and observed that  $\alpha$ SMA was abundantly expressed in Cluster 0, identifying that cluster as a population enriched in myofibroblasts (Figures 5G and 5H). We observed that the number of myofibroblasts (defined as fibroblasts expressing  $\alpha$ SMA) (Cluster 0) was significantly increased by 33% in the *Col5a1*CKO animals (Figure 5I). To confirm these findings, we performed double immunofluorescence staining for  $\alpha$ SMA and vimentin (fibroblast marker) on hearts of *Col5a1*CKO mice and observed that the number of myofibroblasts (defined as the fraction of  $\alpha$ SMA+vimentin+/total

#### Figure 4. Importance of *Col5a1* in Regulating Cardiac Function Post Injury vis-à-vis Other ECM Genes

(A) HMDP comprising 96 strains of mice were subjected to continuous isoproterenol infusion for 3 weeks.

(B) Gene X trait analysis demonstrating strength of association between individual ECM genes and cardiac traits.

(C–G) Scatterplots show correlation of *Col5a1* expression with traits of (C) LVIDs, (D) LVIDD, (E) LV mass, (F) EF, and (G) E/A ratio following isoproterenol injection across all HMDP strains.

(H) Strength of association between *Col5a1* expression and that of ECM genes (\* $p < 0.01$ ).

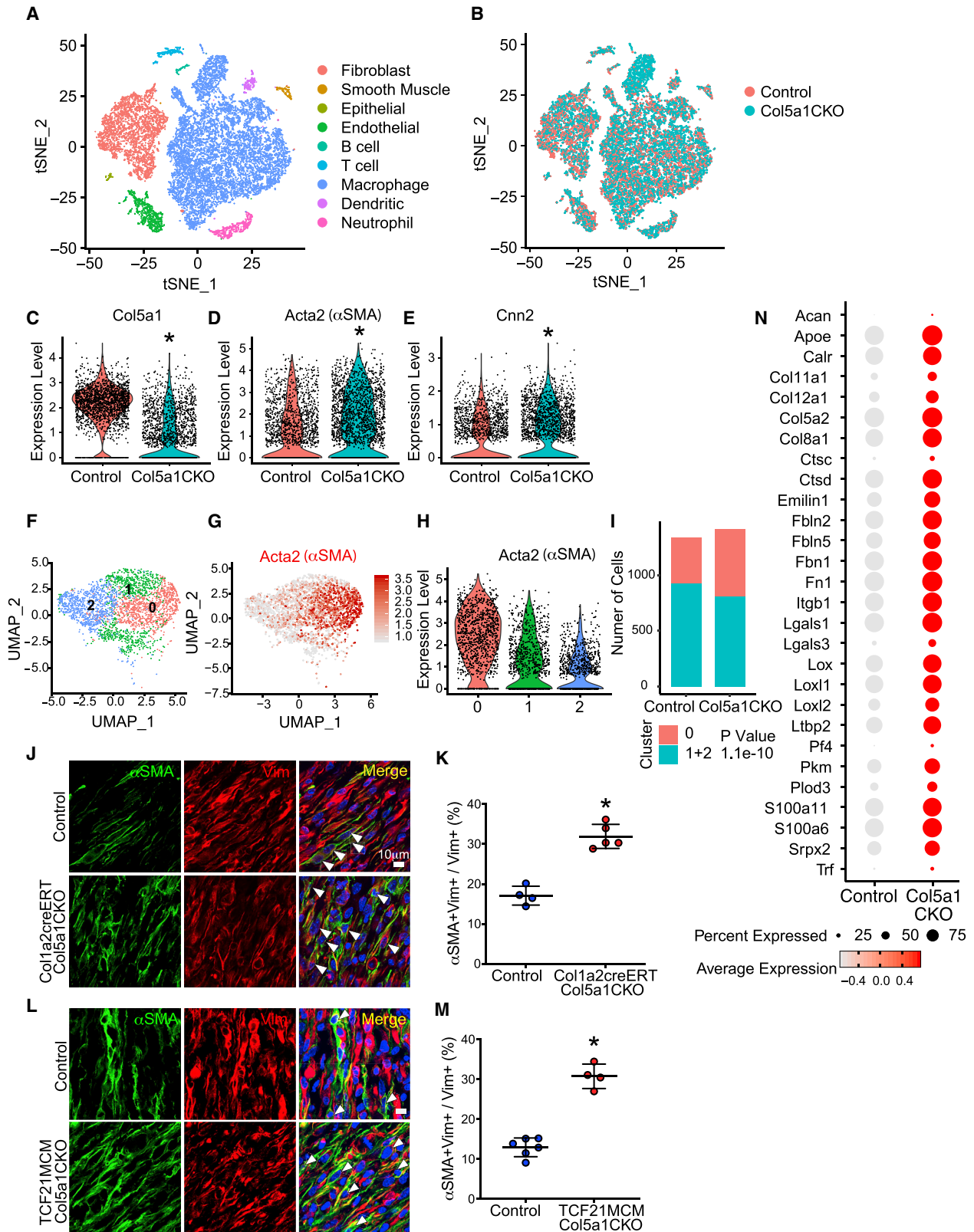
(I) Hypothesis of how adjustment for *Col5a1* could significantly change the strength of association between ECM genes and cardiac traits.

(J) Conditional analysis demonstrating the strength of correlation ( $-\log p$  value) between ECM genes and different cardiac traits following adjustment for *Col5a1* expression (\*\* $p < 0.005$ , \*\* $p < 0.01$ , compared to isoproterenol unadjusted).

(K–N) Change in significance of rest of ECM genes and specific trait (K) LVIDs, (L) LVIDD, (M) LV mass, and (N) EF following adjustment for specific gene (horizontal dotted line shows a cut-off  $p$  value = 0.01).

See also Figure S4.





(legend on next page)

number of vimentin+ cells) was 2- to 2.5-fold greater in the scar tissue of Col5a1CKO mice (Figures 5J and 5K) or that of Tcf21MCM:Col5a1CKO mice (Figures 5L and 5M) (mean  $\pm$  SD, \* $p < 0.05$ ). Analysis of differentially expressed ECM genes demonstrated a large number of ECM genes to be significantly upregulated in Col5a1CKO fibroblasts, including several collagens (*Col8a1* and *Col11a1*), *fibronectin*, *osteopontin*, and *fibrillin* (Figure 5N). Our data suggest that increased numbers of myofibroblasts along with increased expression of myofibroblast markers and other ECM genes in cardiac scar tissue of Col5a1CKO animals contribute to the increase in scar size. We next determined whether increased myofibroblast numbers in Col5a1CKO scar tissue were secondary to increased proliferation. We examined the expression of cell cycle genes that regulate S/G1 as well as G2/M transitions of the cell cycle in cluster 0 (myofibroblast population) (Figures S6A and S6B), but the average expression of such genes did not show any difference between the myofibroblasts of control and Col5a1CKO animals (Figure S6C). We performed immunostaining for a marker of proliferation (Ki67), but also did not observe any significant differences between the fraction of fibroblasts expressing Ki67 (Figure S6D). Collectively, these observations suggest that increased myofibroblast differentiation or formation, rather than myofibroblast proliferation, likely underlies the increased myofibroblast numbers observed in Col5a1CKO scar tissue compared to that of control littermates.

### Collagen V Deficiency Alters Mechanical Properties of Fibroblasts and Matrix in Scar Tissue

We next explored the molecular underpinnings of increased myofibroblast differentiation and hypothesized that altered mechanical properties of the matrix could be driving feedback cues to drive myofibroblast differentiation. We first performed atomic force microscopy (AFM) to determine the stiffness of mid-ventricular scar tissue 7 days post injury and observed that the Young's modulus was significantly decreased by 15% in the Col5a1CKO animals (Figures 6A–6D) and a less-stiff scar is more prone to expansion by hemodynamic forces. Scar contraction is another major determinant of scar size. During wound healing, contractile forces generated by cardiac fibroblasts shrink the size of the scar, but if the surrounding matrix is less stiff, this would decrease the forces transduced through scar tissue. We explored this hypothesis by examining force

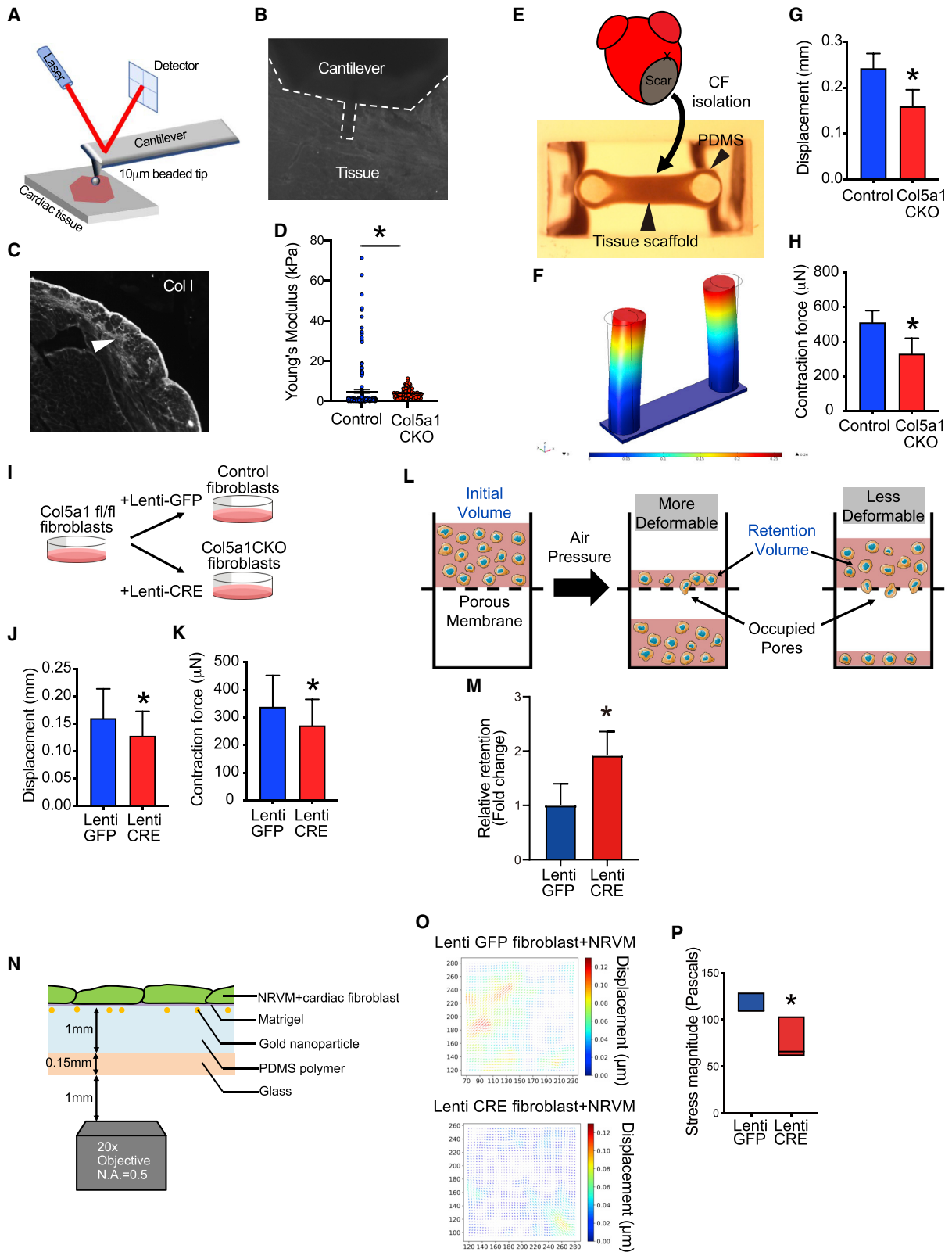
contraction relationships of mutant and control fibroblasts isolated from scar tissue at 7 days following injury. We fabricated a device with polydimethyl siloxane (PDMS) posts, isolated cardiac fibroblasts from infarcted hearts, incorporated the fibroblasts into a collagen hydrogel to form tissue scaffolds, and subsequently suspended the fibroblast-embedded hydrogel between two PDMS posts (Figure 6E). We observed a significantly lower displacement of the PDMS posts with the Col5a1CKO fibroblasts that reflects decreased contractile ability of Col5a1CKO fibroblasts (approximately 34% reduction, \* $p < 0.05$ ) (Figures 6F–6H). Next, we isolated cardiac fibroblasts from Col5a1 floxed mice and infected the cardiac fibroblasts *in vitro* with a lentivirus encoding Cre recombinase gene or GFP as control (Figure 6I). To minimize artifacts from repeated passaging, we immortalized the isolated Col5a1fl/fl cardiac fibroblasts by infecting them with a lentivirus encoding the SV40 large T cell antigen prior to infecting the cells with Cre recombinase or control GFP virus (Mali et al., 2008; Welm et al., 2008). Cells infected by Cre recombinase lentivirus (Truitt et al., 2016) were identified by co-expression of GFP fluorescence and sorted by flow cytometry, and we found an approximately 60%  $\pm$  20% decrease in *Col5a1* expression (mean  $\pm$  SD, \* $p < 0.05$ ). Successfully transduced cells were then incorporated into collagen hydrogels and suspended between PDMS posts in a similar manner. We observed a significant reduction in pillar displacement and hydrogel contraction, suggestive that the deficiency of ColV is sufficient to affect fibroblast contractile forces (Figures 6J and 6K). Taken together, these experiments show that ColV depletion leads to decreased scar stiffness and attenuated tissue scaffold contraction by fibroblasts, which could both contribute to increased scar size.

To assay the mechanical properties of fibroblasts, we subjected the Col5a1floxed cardiac fibroblasts (following lenti Cre infection) to a cell deformability assay. In this assay, cell deformability is determined by parallel microfiltration (PMF), where the ability of cells to filter through a porous membrane over the time-scale of seconds in response to an applied pressure is determined (Kim et al., 2016, 2019; Qi et al., 2015). More deformable cells will filter more quickly through the pores, resulting in a lower volume of cell suspension retained in the top well (Figure 6L). We observed that Col5a1CKO fibroblasts are significantly less deformable (Figure 6M), while there were no significant differences in cell size or viability between lenti Cre or lenti GFP

### Figure 5. Single-Cell RNA-Seq of Non-myocytes of Control and Col5a1CKO Hearts Harvested at 7 Days following Injury

- (A) tSNE plot demonstrating non-myocyte cell populations of the heart at 7 days post MI.  
(B) Distribution of non-myocyte cells from injured control and Col5a1CKO hearts across these clusters.  
(C–E) Violin plot demonstrating expression of (C) Col5a1, (D) Acta2 ( $\alpha$ SMA), and (E) Cnn2 (Calponin) in fibroblast clusters.  
(F) Sub-clustering of fibroblast population.  
(G) UMAP plot with expression of  $\alpha$ SMA in fibroblast subclusters.  
(H) Expression of Acta2 in subclusters of fibroblasts.  
(I) Cell numbers in cluster 0 (myofibroblasts) versus clusters 1 and 2 (non-myofibroblasts).  
(J) Immunostaining for  $\alpha$ smooth muscle actin ( $\alpha$ SMA) and vimentin (Vim) in the scar of Col5a1CKO at 7 days post MI (arrows, representative images).  
(K) Quantitation of the number of  $\alpha$ SMA expressing myofibroblasts ( $n = 4$ /control and 5/CKO).  
(L) Immunostaining for  $\alpha$ SMA and Vim in the scar of TCF21MCM:Col5a1CKO hearts at 7 days post MI (arrows, representative images).  
(M) Quantitation of the number of  $\alpha$ SMA expressing myofibroblasts ( $n = 6$ /control and 4/CKO).  
(N) Dot plot representing expression of ECM genes that are significantly upregulated in fibroblasts of Col5a1CKO hearts at 7 days post MI (adjusted  $p$  value  $< 0.05$ ). Data shown as mean  $\pm$  SD, \* $p < 0.05$ .

See also Figures S5 and S6.



(legend on next page)

cardiac fibroblasts (Figures S7A and S7B). To further investigate the altered physical properties of Col5a1CKO fibroblasts, we performed quantitative phase microscopy (QPM) to measure the rate at which biomass redistributes within individual cells (decorrelation rate). We observed that the decorrelation rate was faster (approximately 2-fold higher) in Col5a1CKO fibroblasts versus control-GFP virus infected fibroblasts; mean  $\pm$  SD, \* $p < 0.05$ ) (Figures S7C–S7E), further substantiating the altered physical properties of Col5a1CKO fibroblasts.

We next examined whether stiffer cardiac fibroblasts affect cardiomyocyte contractile forces, thereby reducing cardiac function. We co-cultured neonatal rodent ventricular cardiomyocytes (NRVMs) with Col5a1-deficient or control cardiac fibroblasts generated *in vitro*. We performed traction force microscopy to determine myocyte contractile forces generated in the presence of control or Col5a1CKO cardiac fibroblasts. A co-culture of cardiomyocytes and control or Col5a1CKO cardiac fibroblasts was seeded onto a Matrigel surface on a PDMS scaffold containing gold-labeled nano-particles (Figure 6N). As the myocytes contract, the movement or displacement of the gold particles is captured, and machine learning approaches are utilized to calculate contractile forces (Figure 6O). Using this approach, we observed that the stress generated by myocytes in the presence of Col5a1CKO fibroblasts is significantly decreased (mean  $\pm$  SD, \* $p < 0.05$ ) (Figure 6P). These observations are consistent with our *in vivo* findings of decreased cardiac contractile forces in Col5a1CKO hearts following ischemic cardiac injury.

### Collagen V Deficiency Induces Myofibroblast Formation via Altered Integrin Expression on Cardiac Fibroblasts

Given the abnormal biomechanical properties of the scar, we hypothesized that altered mechanical cues were driving a myofibroblast gene expression program and increasing myofibroblast formation. First, we determined whether the deficiency of Col5a1 in cardiac fibroblasts was sufficient to induce myofibroblast differentiation and expression of ECM genes. To address this question, we again generated Col5a1-deficient cardiac fibroblasts by lentiviral Cre transduction and observed significant upregulation of canonical myofibroblast and ECM genes such as  $\alpha$ SMA, *perioxin*, *Col3a1*, *Myh11*, etc. (Figure 7A). These observations demonstrate that the loss of *Col5a1* is sufficient to induce activa-

tion of a myofibroblast gene expression program. Integrins are mechanosensitive receptors on the cell surface, and alterations in mechanical properties of the extracellular environment can lead to rapid changes in integrin profile. Moreover, integrins are known to regulate key cellular events such as cell survival, proliferation, and differentiation (Hynes, 2002; Katsumi et al., 2004). We hypothesized that augmentation of a myofibroblast gene expression program in Col5a1CKO fibroblasts could be secondary to altered integrin expression on the Col5a1CKO fibroblasts. We performed flow cytometry on Col5a1-deficient cardiac fibroblasts and observed that a significantly greater fraction of Col5a1-deficient cardiac fibroblasts expressed the integrins  $\alpha$ v $\beta$ 3 and  $\alpha$ v $\beta$ 5 (Figures 7B and 7C). In contrast,  $\beta$ 1,  $\beta$ 2,  $\alpha$ 5, and  $\alpha$ v integrins did not show any changes in expression (Figures S7F–S7I). These integrins were chosen as they have shown to affect smooth muscle and fibroblast function (Deb et al., 2004; Ieda et al., 2009; Liu et al., 2010), and particularly for  $\alpha$ v $\beta$ 3/ $\alpha$ v $\beta$ 5, there is evidence that these integrins promote myofibroblast differentiation by modulating latent TGF $\beta$  signaling (Asano et al., 2005; Lygoe et al., 2004; Sarrazy et al., 2014).

Immunostaining demonstrated robust expression of  $\alpha$ v $\beta$ 3 and  $\alpha$ v $\beta$ 5 integrins in cardiac fibroblasts of Col5a1CKO scar tissue compared to that of control littermates (Figures 7D and 7E). Myocardium remote to the area of injury did not show any expression of  $\alpha$ v $\beta$ 3 and  $\alpha$ v $\beta$ 5 integrins (Figure S8A). Given the upregulation of  $\alpha$ v $\beta$ 3 and  $\alpha$ v $\beta$ 5 integrins in Col5a1CKO cardiac fibroblasts, we next determined whether there was a causal relationship between these differentially expressed integrins and myofibroblast differentiation. To address this question, we adopted a pharmacologic loss-of-function approach by using the drug cilengitide, a specific inhibitor of  $\alpha$ v $\beta$ 3 and  $\alpha$ v $\beta$ 5 integrins. Cilengitide is a cyclic Arg-Gly-Asp peptide that has been used in human clinical trials of various malignancies, such as gliomas, and is a specific inhibitor of the  $\alpha$ v $\beta$ 3 and  $\alpha$ v $\beta$ 5 integrins (Belvisi et al., 2005; Dechantsreiter et al., 1999; Scaringi et al., 2012). We infected the Col5a1 floxed cardiac fibroblasts with a lentiviral Cre or control GFP and added cilengitide to cardiac fibroblasts at the same time. After 7 days, expression of myofibroblast markers was significantly increased in the Col5a1CKO fibroblasts, but the addition of cilengitide significantly reduced expression of myofibroblast markers (Figure 7F).

### Figure 6. Col5a1CKO Fibroblasts Exhibit Altered Mechano-biological Properties

(A) Schematic illustration of atomic force microscopy (AFM) instrumentation.

(B) Representative image of AFM probe and cantilever over tissue section.

(C) Representative image of collagen I (Col I) indirect immunofluorescence detection in scar region (arrow) that was probed with AFM.

(D) Young's Modulus measurements from injured regions (mean  $\pm$  SEM, \* $p < 0.05$ ,  $n = 3$ ).

(E–H) Determination of mutant or control cardiac fibroblasts (CFs) to generate contractile forces. (E) CFs were isolated at 7 days post MI and incorporated into hydrogel scaffolds and suspended between PDMS posts. (F) Contraction of CFs determined from displacement of PDMS posts. (G) Displacement of PDMS posts by CF tissue scaffold ( $n = 3$ ). (H) Contraction forces generated by either control or Col5a1CKO CFs ( $n = 3$ ).

(I–K) Determination of contractile forces by generating Col5a1CKO CFs *ex vivo*. (I) CFs from hearts of Col5a1fl/fl mice were infected with a lentiviral Cre or GFP virus to create Col5a1 deficient CFs. (J) Displacement of the PDMS posts and (K) contractile forces generated by Col5a1CKO CFs ( $n = 3$ ).

(L) Schematic illustration of parallel microfiltration (PMF) assay.

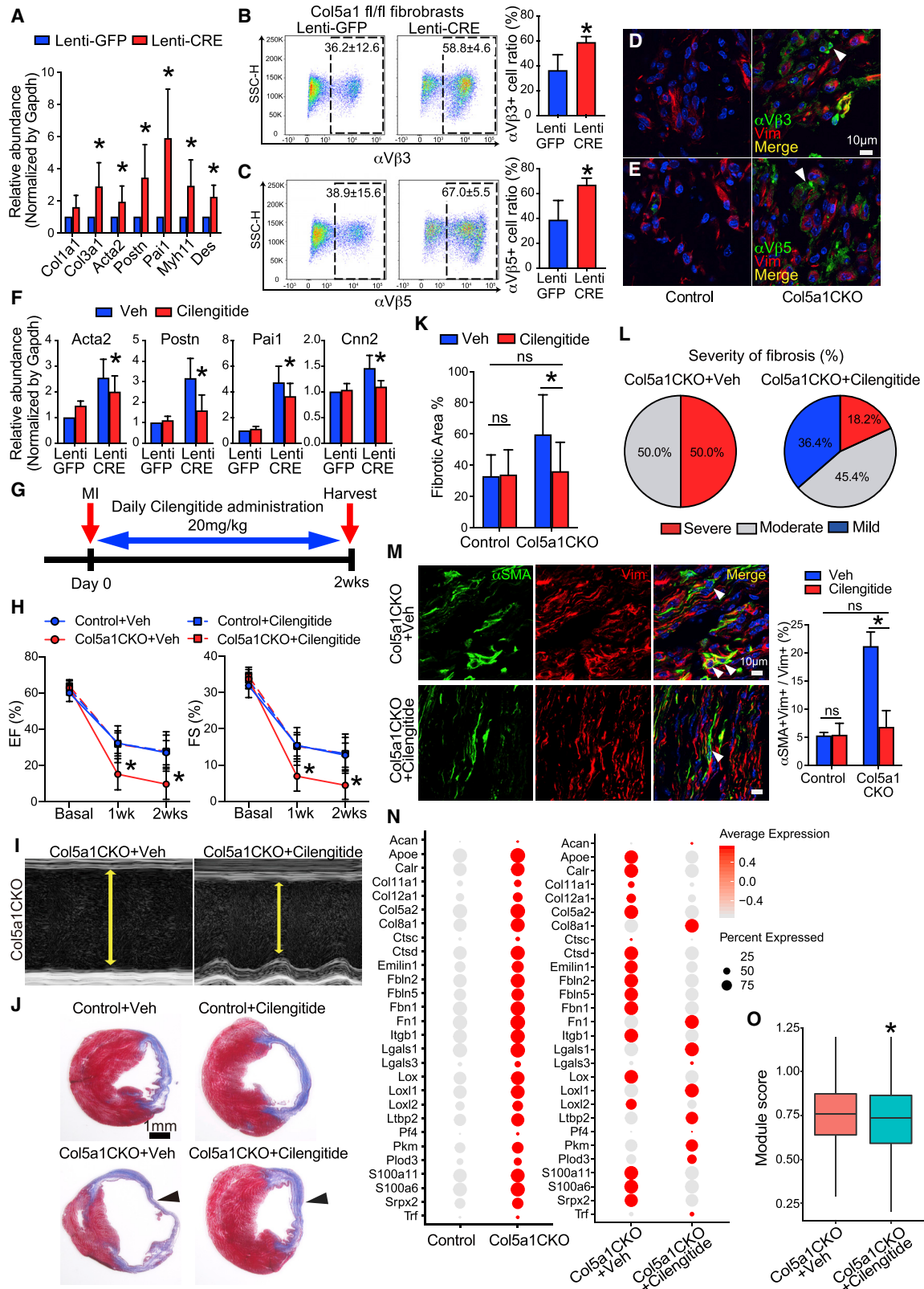
(M) Relative retention of cells measured by PMF assay and normalized to the control (Lenti-GFP) CFs ( $n = 3$ ).

(N) Schematic of set up of traction force microscopy where myocytes and CFs are seeded onto a matrigel layer containing gold-labeled nanoparticles.

(O and P) Heatmaps demonstrate displacement of clusters of contracting myocytes (O) and determination of stress forces generated by myocytes in the presence of Col5a1CKO CFs (P) ( $n = 3$ ). Data, unless otherwise stated, shown as mean  $\pm$  SD, \* $p < 0.05$ .

See also Figure S7.





(legend on next page)

Considering these observations, we investigated the effects of injecting cilengitide *in vivo* to Col5a1CKO animals to determine effects on post-injury scar size and cardiac function. We subjected Col5a1CKO to ischemic cardiac injury and injected cilengitide or vehicle at 20mg/kg daily (Bagnato et al., 2018) for 14 days starting from the day of injury (Figure 7G). We observed that the Col5a1CKO animals injected with vehicle exhibited a significant decline in post-injury cardiac function, but the Col5a1CKO animals treated with cilengitide had a complete rescue of function and the post-injury heart function was not significantly different from the control littermates (Cre(-) Col5a1<sup>fl/fl</sup>) (Figures 7H and 7I). In contrast, cilengitide infusion did not affect post-injury cardiac function of control (Cre(-)Col5a1<sup>fl/fl</sup>) littermate animals (Figure 7H). Histology demonstrated significant reduction in scar size in Col5a1CKO animals injected with cilengitide compared to vehicle-injected Col5a1CKO animals (Figures 7J and 7K). To demonstrate that the benefits of cilengitide on post-injury cardiac function of Col5a1CKO animals was secondary to its effect on the infarcted region, we performed myocardial strain imaging. Longitudinal strain generated by different segments of myocardial walls is a surrogate for contractile forces generated. With MI, the basal segment of the myocardium close to the suture line was relatively unaffected compared to the anterior apical wall (Figures S8B and S8C). Following cilengitide administration, the functional improvement was restricted to the apical segment and not the basal segment, demonstrating that the beneficial effects of cilengitide were not secondary to augmentation of contractile forces of the non-injured myocardium (Figure S8D). Cilengitide did not affect the scar size of control animals (Cre(-)Col5a1<sup>fl/fl</sup>) following injury (Figures 7J and 7K). The Col5a1CKO animals injected with cilengitide had a much lower fraction of animals exhibiting severe fibrosis (Figure 7L). We next examined the numbers of myofibroblasts in the scars of Col5a1CKO animals and observed that the number of myofibroblasts was significantly reduced in the cilengitide group (Figure 7M). We subsequently determined whether cilengitide reversed increased expression of ECM genes in cardiac fibroblasts of Col5a1CKO animals. We examined the set of ECM genes that were upregulated in cardiac fibroblasts in Col5a1CKO hearts at 7 days following injury. scRNA-seq of fibro-

blasts isolated from Col5a1CKO hearts following 7 days of cilengitide therapy demonstrated reversion of expression of these genes, and average expression of this module of genes was significantly lower in cardiac fibroblasts following cilengitide treatment ( $p = 9.3e-7$ ) (Figures 7N and 7O). The degree of myocyte hypertrophy was also substantially reduced in the cilengitide-injected Col5a1CKO animals (Figures S8E and S8F). Taken together, these experiments demonstrate that the differential expression of  $\alpha v\beta 3$  and  $\alpha v\beta 5$  integrins in cardiac fibroblasts of Col5a1CKO animals drives myofibroblast differentiation, and pharmacologic inhibition of such integrins is sufficient to rescue the phenotype.

## DISCUSSION

Our data can be used to construct a collagen-V-dependent model of cardiac wound healing where Col V regulates wound healing at least in part by modulating the mechanical properties of the scar. In the absence of Col V, the scar is less stiff, and less stiff scars are prone to sudden scar expansion (Rog-Zielinska et al., 2016). In addition, the reduced scar stiffness drives integrin-mediated mechanical feedback cues that promote myofibroblast differentiation, further ECM production, and scar size. The feedback response is critical to the phenotype as modulation of specific integrin signaling reverses increased ECM gene expression and rescues the phenotype.

Our findings could also have implications for Ehlers Danlos syndrome (EDS), a heterogeneous group of connective tissue disorders characterized by abnormalities in skin extensibility, joint hypermobility, and tissue fragility (Ghali et al., 2019). Individuals with classical EDS (cEDS) most commonly have mutations in genes encoding for type V collagen (Col5a1 and Col5a2) (Wenstrup et al., 2000). Although there is scant clinical data on the prognosis of MI and heart scarring in these patients (owing to the relatively rare nature of the disease), patients with cEDS have abnormal mechanical properties of the ECM and exhibit dysregulated wound healing with increased scar size. Moreover, fibroblasts isolated from skin of patients with cEDS demonstrate increased expression of  $\alpha v\beta 3$  integrins (Zoppi et al., 2018) that is thought to reflect a response to abnormal ECM and raise the

### Figure 7. Inhibition of $\alpha v\beta 3$ and $\alpha v\beta 5$ Integrins Rescues Increased Scarring and Cardiac Dysfunction in Col5a1CKO Animals

- (A) Expression of ECM and myofibroblast genes in Col5a1CKO CFs generated *ex vivo* (n = 6).  
(B and C) Flow cytometry to determine expression of (B)  $\alpha v\beta 3$  and (C)  $\alpha v\beta 5$  integrins on Col5a1CKO CFs (n = 6).  
(D and E) Immunostaining for Vim, (D)  $\alpha v\beta 3$ , and (E)  $\alpha v\beta 5$  in scar tissue at 7 days post MI (arrows, representative images).  
(F) Expression of key myofibroblast genes in Col5a1CKO CFs in the presence or absence of cilengitide (n = 6).  
(G) Experimental design to treat animals with daily cilengitide (20mg/kg).  
(H) EF and FS in control and Col5a1CKO injected with cilengitide or vehicle (\*Col5a1CKO+Cilengitide [red dotted line] versus Col5a1CKO+Veh [red solid line], n = 13/CKO+Cilengitide 10/other groups at basal, n = 12/CKO+Cilengitide, 6/CKO+Veh, 9/Control+Cilengitide, 7/Control+Veh at 2 weeks post MI).  
(I) Representative images of M-mode echocardiogram (yellow line indicates end systolic diameter).  
(J) Masson trichrome staining of mid-ventricle at 2 weeks post MI to show scar size (arrowhead, n = same number at 2 weeks post MI, as above).  
(K) Quantitation of fibrotic area (n = same number as above).  
(L) Fraction of Col5a1CKO animals demonstrating mild, moderate, and severe fibrosis following vehicle or cilengitide infusion  
(M) Immunostaining for  $\alpha$ SMA and Vimentin in hearts of Col5a1CKO receiving vehicle or cilengitide and quantitation of the fraction (arrows, representative images, n = 10/CKO+Cilengitide, n = 6/CKO+Veh, n = 6/animals for all other groups).  
(N) Dot plot representing expression of ECM genes that are upregulated in CFs of Col5a1CKO hearts at 7 days post MI compared to controls (left panel). The same genes were shown in fibroblasts from Col5a1CKO+Vehicle and Col5a1CKO+Cilengitide samples (right panel).  
(O) Boxplot showing the module scores of 28 genes from (N) in fibroblasts from Col5a1CKO+Veh and Col5a1CKO+Cilengitide. Data shown as mean  $\pm$  SD, \* $p < 0.05$ , ns: not significant.

See also Figures S7 and S8.



possibility that inhibitors of specific integrins such as cilengitide may have a role in mitigating dysregulated wound healing in cEDS.

In summary, we demonstrate that a feedback mechanism between the mechanical properties of scar tissue and cardiac fibroblasts are pivotal to the regulation of scar size. Teleologically, such a feedback loop provides an efficient way to integrate the output of ECM and strength of scars. Our observations illustrate a model of wound healing in which the structural constituents of scar tissue function to limit the size of scar itself.

## STAR★METHODS

Detailed methods are provided in the online version of this paper and include the following:

- **KEY RESOURCES TABLE**
- **RESOURCE AVAILABILITY**
  - Lead Contact
  - Materials Availability
  - Data and Code Availability
- **EXPERIMENTAL MODEL AND SUBJECT DETAILS**
  - Animal care and use
  - Generation of animals with genetically labeled cardiac fibroblasts and fibroblast specific deletion of Col5a1
  - Murine models of acute ischemic cardiac injury
  - Echocardiogram
- **METHOD DETAILS**
  - Antibodies and probes
  - Bulk RNA-seq, single-cell RNA-seq and qPCR
  - Col5a1 correlation with extracellular matrix pathway accounts for clinical trait association in the HMDP
  - Proteomic analysis of scar tissue
  - Histological studies
  - RNA-Fluorescence *in situ* hybridization
  - Insoluble collagen assay
  - Transmission electron microscopy
  - Tomography of collagen fibers
  - Plasmid construction and Lentivirus preparation
  - Isolation of primary culture adult cardiac fibroblast
  - Generation of Col5a1 deficient immortalized cardiac fibroblast
  - Flow cytometry
  - Measurement of force generated by Col V deficient cardiac fibroblasts
  - Measurement of decorrelation rate of Col V deficient cardiac fibroblasts
  - Traction force measurement of neonatal rat ventricle myocyte and fibroblast co-culture
  - Parallel microfiltration
  - Atomic force microscopy
- **QUANTIFICATION AND STATISTICAL ANALYSIS**

## SUPPLEMENTAL INFORMATION

Supplemental Information can be found online at <https://doi.org/10.1016/j.cell.2020.06.030>.

## ACKNOWLEDGMENTS

We thank Dr. Eric Olson, University of Texas Southwestern Medical Center and Dr. Andrew Leask, University of Western Ontario, Canada for providing us the TCF21MerCreMer and Col1a2CreERT mice, respectively. We thank Dr. Siobhan Braybrook (UCLA) and Dr. Dan Cohn (UCLA) for AFM and ECM expertise. This work was funded by grants from the National Institutes of Health, U.S.A. (HL129178, HL137241, AR075867, HL126204, and HL147883), Department of Defense, U.S.A. (W81XWH-17-1-0464 and W81XWH-20-1-0238), National Science Foundation, U.S.A. (BMMB-1906165), grants from the Eli and Edythe Broad Stem Cell Center at UCLA and California Nanosystems Institute (BSCRC/CNSI innovation award), and James Eason Cardiovascular Discovery funds. This research was also partly supported by NIH National Center for Advancing Translational Science (NCATS) UCLA Clinical and Translational Science Institute (CTSI), U.S.A. (grant number UL1TR001881). J.L.M. was supported by UPLIFT: UCLA Postdocs' Longitudinal Investment in Faculty (NIH K12 GM106996).

## AUTHOR CONTRIBUTIONS

T.Y. performed the majority of experiments and analyzed data including cardiac imaging. S.L., Y.Z., R.W., and A.R. assisted in bench experiments. S.R. and Y.W. performed animal surgeries. Y.Z.K., F.M., and M.P. analyzed RNA-seq and scRNA-seq. J.M. and R.H.C. performed, analyzed, and interpreted AFM experiments. T.N. and M.A.T. performed and analyzed QPM experiments. T.-H.K. and A.C.R. performed and interpreted PMF experiments. X.H.M.T. and P.Y.-C. performed and interpreted traction force microscopy experiments. R.N., S.A., and A.K. performed and analyzed contraction of tissue scaffolds. W.C. and J.W. performed mass spectroscopy experiments. M.S. and A.J.L. analyzed HMDP data. S.R. performed TEM. D.E.B. provided key reagents and contributed toward discussion. A.D. conceptualized the project, supervised data collection and analysis, and wrote the manuscript.

## DECLARATION OF INTERESTS

The authors declare no competing interests. Based on this work, patent no: 63/002,828 "Compositions and methods for treating dysregulated wound healing" has been filed and assigned to the Regents of the University of California.

Received: November 15, 2019

Revised: March 17, 2020

Accepted: June 18, 2020

Published: July 3, 2020

## REFERENCES

- Acharya, A., Baek, S.T., Banfi, S., Eskiocak, B., and Tallquist, M.D. (2011). Efficient inducible Cre-mediated recombination in Tcf21 cell lineages in the heart and kidney. *Genesis* 49, 870–877.
- Asano, Y., Ihn, H., Yamane, K., Jinnin, M., Mimura, Y., and Tamaki, K. (2005). Increased expression of integrin alpha(v)beta3 contributes to the establishment of autocrine TGF-beta signaling in scleroderma fibroblasts. *J. Immunol.* 175, 7708–7718.
- Bagnato, G.L., Irrera, N., Pizzino, G., Santoro, D., Roberts, W.N., Bagnato, G., Pallio, G., Vaccaro, M., Squadrito, F., Saitta, A., et al. (2018). Dual  $\alpha v \beta 3$  and  $\alpha v \beta 5$  blockade attenuates fibrotic and vascular alterations in a murine model of systemic sclerosis. *Clin. Sci. (Lond.)* 132, 231–242.
- Barer, R. (1952). Interference microscopy and mass determination. *Nature* 169, 366–367.
- Bashey, R.I., Martinez-Hernandez, A., and Jimenez, S.A. (1992). Isolation, characterization, and localization of cardiac collagen type VI. Associations with other extracellular matrix components. *Circ. Res.* 70, 1006–1017.
- Belvisi, L., Riccioni, T., Marcellini, M., Vesce, L., Chiarucci, I., Efrati, D., Potenza, D., Scolastico, C., Manzoni, L., Lombardo, K., et al. (2005). Biological and molecular properties of a new alpha(v)beta3/alpha(v)beta5 integrin antagonist. *Mol. Cancer Ther.* 4, 1670–1680.

- Bendat, J.S., and Piersol, A.G. (2013). Random data: analysis and measurement procedures (Wiley-Interscience).
- Beussman, K.M., Rodriguez, M.L., Leonard, A., Taparia, N., Thompson, C.R., and Sniadecki, N.J. (2016). Micropost arrays for measuring stem cell-derived cardiomyocyte contractility. *Methods* 94, 43–50.
- Bon, P., Maucort, G., Wattellier, B., and Monneret, S. (2009). Quadriwave lateral shearing interferometry for quantitative phase microscopy of living cells. *Opt. Express* 17, 13080–13094.
- Brown, X.Q., Ookawa, K., and Wong, J.Y. (2005). Evaluation of polydimethylsiloxane scaffolds with physiologically-relevant elastic moduli: interplay of substrate mechanics and surface chemistry effects on vascular smooth muscle cell response. *Biomaterials* 26, 3123–3129.
- Crocker, J.C., and Grier, D.G. (1996). Methods of digital video microscopy for colloidal studies. *J. Colloid Interface Sci.* 179, 298–310.
- Davies, H.G., and Wilkins, M.H. (1952). Interference microscopy and mass determination. *Nature* 169, 541.
- Deb, A., Skelding, K.A., Wang, S., Reeder, M., Simper, D., and Caplice, N.M. (2004). Integrin profile and in vivo homing of human smooth muscle progenitor cells. *Circulation* 110, 2673–2677.
- Dechantsreiter, M.A., Planker, E., Mathä, B., Lohof, E., Hölzemann, G., Jonczyk, A., Goodman, S.L., and Kessler, H. (1999). N-Methylated cyclic RGD peptides as highly active and selective alpha(V)beta(3) integrin antagonists. *J. Med. Chem.* 42, 3033–3040.
- Dobin, A., Davis, C.A., Schlesinger, F., Drenkow, J., Zaleski, C., Jha, S., Batut, P., Chaisson, M., and Gingeras, T.R. (2013). STAR: ultrafast universal RNA-seq aligner. *Bioinformatics* 29, 15–21.
- Frangogiannis, N.G. (2017). The extracellular matrix in myocardial injury, repair, and remodeling. *J. Clin. Invest.* 127, 1600–1612.
- Frangogiannis, N.G. (2019). The Extracellular Matrix in Ischemic and Nonischemic Heart Failure. *Circ. Res.* 125, 117–146.
- Ghali, N., Sobey, G., and Burrows, N. (2019). Ehlers-Danlos syndromes. *BMJ* 366, i4966.
- Ghazalpour, A., Rau, C.D., Farber, C.R., Bennett, B.J., Orozco, L.D., van Nas, A., Pan, C., Allayee, H., Beaven, S.W., Civelek, M., et al. (2012). Hybrid mouse diversity panel: a panel of inbred mouse strains suitable for analysis of complex genetic traits. *Mamm. Genome* 23, 680–692.
- Gulati, A., Jabbour, A., Ismail, T.F., Guha, K., Khwaja, J., Raza, S., Morarji, K., Brown, T.D., Ismail, N.A., Dweck, M.R., et al. (2013). Association of fibrosis with mortality and sudden cardiac death in patients with nonischemic dilated cardiomyopathy. *JAMA* 309, 896–908.
- Heras-Bautista, C.O., Mikhael, N., Lam, J., Shinde, V., Katsen-Globa, A., Diel-uwweit, S., Molcanyi, M., Uvarov, V., Jütten, P., Sahito, R.G.A., et al. (2019). Cardiomyocytes facing fibrotic conditions re-express extracellular matrix transcripts. *Acta Biomater.* 89, 180–192.
- Hinkel, R., Ball, H.L., DiMaio, J.M., Shrivastava, S., Thatcher, J.E., Singh, A.N., Sun, X., Faskerti, G., Olson, E.N., Kupatt, C., and Bock-Marquette, I. (2015). C-terminal variable AGES domain of Thymosin  $\beta$ 4: the molecule's primary contribution in support of post-ischemic cardiac function and repair. *J. Mol. Cell. Cardiol.* 87, 113–125.
- Hynes, R.O. (2002). Integrins: bidirectional, allosteric signaling machines. *Cell* 110, 673–687.
- Ieda, M., Tsuchihashi, T., Ivey, K.N., Ross, R.S., Hong, T.T., Shaw, R.M., and Srivastava, D. (2009). Cardiac fibroblasts regulate myocardial proliferation through beta1 integrin signaling. *Dev. Cell* 16, 233–244.
- Kanisicak, O., Khalil, H., Ivey, M.J., Karch, J., Maliken, B.D., Correll, R.N., Brody, M.J., J Lin, S.C., Aronow, B.J., Tallquist, M.D., and Molkentin, J.D. (2016). Genetic lineage tracing defines myofibroblast origin and function in the injured heart. *Nat. Commun.* 7, 12260.
- Katsumi, A., Orr, A.W., Tzima, E., and Schwartz, M.A. (2004). Integrins in mechanotransduction. *J. Biol. Chem.* 279, 12001–12004.
- Kim, T.H., Gill, N.K., Nyberg, K.D., Nguyen, A.V., Hohlbauch, S.V., Geisse, N.A., Nowell, C.J., Sloan, E.K., and Rowat, A.C. (2016). Cancer cells become less deformable and more invasive with activation of  $\beta$ -adrenergic signaling. *J. Cell Sci.* 129, 4563–4575.
- Kim, T.H., Ly, C., Christodoulides, A., Nowell, C.J., Gunning, P.W., Sloan, E.K., and Rowat, A.C. (2019). Stress hormone signaling through  $\beta$ -adrenergic receptors regulates macrophage mechanotype and function. *FASEB J.* 33, 3997–4006.
- Kremer, J.R., Mastronarde, D.N., and McIntosh, J.R. (1996). Computer visualization of three-dimensional image data using IMOD. *J. Struct. Biol.* 116, 71–76.
- Lincoln, J., Florer, J.B., Deutsch, G.H., Wenstrup, R.J., and Yutzey, K.E. (2006). ColVa1 and ColXla1 are required for myocardial morphogenesis and heart valve development. *Dev. Dyn.* 235, 3295–3305.
- Liu, S., Xu, S.W., Blumbach, K., Eastwood, M., Denton, C.P., Eckes, B., Krieg, T., Abraham, D.J., and Leask, A. (2010). Expression of integrin beta1 by fibroblasts is required for tissue repair in vivo. *J. Cell Sci.* 123, 3674–3682.
- Lusis, A.J., Seldin, M.M., Allayee, H., Bennett, B.J., Civelek, M., Davis, R.C., Eskin, E., Farber, C.R., Hui, S., Mehrabian, M., et al. (2016). The Hybrid Mouse Diversity Panel: a resource for systems genetics analyses of metabolic and cardiovascular traits. *J. Lipid Res.* 57, 925–942.
- Lygoe, K.A., Norman, J.T., Marshall, J.F., and Lewis, M.P. (2004). AlphaV integrins play an important role in myofibroblast differentiation. *Wound Repair Regen.* 12, 461–470.
- Ma, X., Dewan, S., Liu, J., Tang, M., Miller, K.L., Yu, C., Lawrence, N., McCulloch, A.D., and Chen, S. (2019). 3D printed micro-scale force gauge arrays to improve human cardiac tissue maturation and enable high throughput drug testing. *Acta Biomater.* 95, 319–327.
- Mali, P., Ye, Z., Hommond, H.H., Yu, X., Lin, J., Chen, G., Zou, J., and Cheng, L. (2008). Improved efficiency and pace of generating induced pluripotent stem cells from human adult and fetal fibroblasts. *Stem Cells* 26, 1998–2005.
- Otsu, N. (1979). Threshold Selection Method from Gray-Level Histograms. *IEEE Transactions on Systems, Man, and Cybernetics* 9, 62–66.
- Oyunbaatar, N.E., Lee, D.H., Patil, S.J., Kim, E.S., and Lee, D.W. (2016). Biomechanical Characterization of Cardiomyocyte Using PDMS Pillar with Microgrooves. *Sensors (Basel)* 16. <https://doi.org/10.3390/s16081258>.
- Pettersen, E.F., Goddard, T.D., Huang, C.C., Couch, G.S., Greenblatt, D.M., Meng, E.C., and Ferrin, T.E. (2004). UCSF Chimera—a visualization system for exploratory research and analysis. *J. Comput. Chem.* 25, 1605–1612.
- Pillai, I.C., Li, S., Romay, M., Lam, L., Lu, Y., Huang, J., Dillard, N., Zemanova, M., Rubbi, L., Wang, Y., et al. (2017). Cardiac Fibroblasts Adopt Osteogenic Fates and Can Be Targeted to Attenuate Pathological Heart Calcification. *Cell Stem Cell* 20, 218–232.e5.
- Qi, D., Kaur Gill, N., Santiskulvong, C., Sifuentes, J., Dorigo, O., Rao, J., Taylor-Harding, B., Ruprecht Wiedemeyer, W., and Rowat, A.C. (2015). Screening cell mechanotype by parallel microfiltration. *Sci. Rep.* 5, 17595.
- Rappilber, J., Mann, M., and Ishihama, Y. (2007). Protocol for micro-purification, enrichment, pre-fractionation and storage of peptides for proteomics using StageTips. *Nat. Protoc.* 2, 1896–1906.
- Rau, C.D., Wang, J., Avetisyan, R., Romay, M.C., Martin, L., Ren, S., Wang, Y., and Lusis, A.J. (2015). Mapping genetic contributions to cardiac pathology induced by Beta-adrenergic stimulation in mice. *Circ Cardiovasc Genet* 8, 40–49.
- Rau, C.D., Romay, M.C., Tuteryan, M., Wang, J.J., Santolini, M., Ren, S., Karma, A., Weiss, J.N., Wang, Y., and Lusis, A.J. (2017). Systems Genetics Approach Identifies Gene Pathways and Adamts2 as Drivers of Isoproterenol-Induced Cardiac Hypertrophy and Cardiomyopathy in Mice. *Cell Syst.* 4, 121–128.e4.
- Ren, J., Zhang, S., Kovacs, A., Wang, Y., and Muslin, A.J. (2005). Role of p38alpha MAPK in cardiac apoptosis and remodeling after myocardial infarction. *J. Mol. Cell. Cardiol.* 38, 617–623.
- Ribeiro, A.J., Denisin, A.K., Wilson, R.E., and Pruitt, B.L. (2016). For whom the cells pull: Hydrogel and micropost devices for measuring traction forces. *Methods* 94, 51–64.

- Robinson, M.D., McCarthy, D.J., and Smyth, G.K. (2010). edgeR: a Bioconductor package for differential expression analysis of digital gene expression data. *Bioinformatics* 26, 139–140.
- Rog-Zielinska, E.A., Norris, R.A., Kohl, P., and Markwald, R. (2016). The Living Scar–Cardiac Fibroblasts and the Injured Heart. *Trends Mol. Med.* 22, 99–114.
- Sarrazy, V., Koehler, A., Chow, M.L., Zimina, E., Li, C.X., Kato, H., Caldarone, C.A., and Hinz, B. (2014). Integrins  $\alpha\text{v}\beta 5$  and  $\alpha\text{v}\beta 3$  promote latent TGF- $\beta 1$  activation by human cardiac fibroblast contraction. *Cardiovasc. Res.* 102, 407–417.
- Scaringi, C., Minniti, G., Caporello, P., and Enrici, R.M. (2012). Integrin inhibitor cilengitide for the treatment of glioblastoma: a brief overview of current clinical results. *Anticancer Res.* 32, 4213–4223.
- Sneddon, I.N. (1965). The relation between load and penetration in the axisymmetric boussinesq problem for a punch of arbitrary profile. *International Journal of Engineering Science* 3, 47–57.
- Sun, M., Chen, S., Adams, S.M., Florer, J.B., Liu, H., Kao, W.W., Wenstrup, R.J., and Birk, D.E. (2011). Collagen V is a dominant regulator of collagen fibrillogenesis: dysfunctional regulation of structure and function in a corneal-stroma-specific Col5a1-null mouse model. *J. Cell Sci.* 124, 4096–4105.
- Truitt, J.M., Blednov, Y.A., Benavidez, J.M., Black, M., Ponomareva, O., Law, J., Merriman, M., Horani, S., Jameson, K., Lasek, A.W., et al. (2016). Inhibition of IKK $\beta$  Reduces Ethanol Consumption in C57BL/6J Mice. *eNeuro* 3. <https://doi.org/10.1523/ENEURO.0256-16.2016>.
- Ubil, E., Duan, J., Pillai, I.C., Rosa-Garrido, M., Wu, Y., Bargiacchi, F., Lu, Y., Stanboully, S., Huang, J., Rojas, M., et al. (2014). Mesenchymal-endothelial transition contributes to cardiac neovascularization. *Nature* 514, 585–590.
- van den Borne, S.W., Diez, J., Blankesteijn, W.M., Verjans, J., Hofstra, L., and Narula, J. (2010). Myocardial remodeling after infarction: the role of myofibroblasts. *Nat. Rev. Cardiol.* 7, 30–37.
- Wang, Z., Volinsky, A.A., and Gallant, N.D. (2014). Crosslinking effect on polydimethylsiloxane elastic modulus measured by custom-built compression instrument. *J. Appl. Polym. Sci.* 131.
- Wang, J.J., Rau, C., Avetisyan, R., Ren, S., Romay, M.C., Stolin, G., Gong, K.W., Wang, Y., and Lusic, A.J. (2016). Genetic Dissection of Cardiac Remodeling in an Isoproterenol-Induced Heart Failure Mouse Model. *PLoS Genet.* 12, e1006038.
- Weber, K.T. (1989). Cardiac interstitium in health and disease: the fibrillar collagen network. *J. Am. Coll. Cardiol.* 13, 1637–1652.
- Welm, B.E., Dijkgraaf, G.J., Bledau, A.S., Welm, A.L., and Werb, Z. (2008). Lentiviral transduction of mammary stem cells for analysis of gene function during development and cancer. *Cell Stem Cell* 2, 90–102.
- Wenstrup, R.J., Florer, J.B., Willing, M.C., Giunta, C., Steinmann, B., Young, F., Susic, M., and Cole, W.G. (2000). COL5A1 haploinsufficiency is a common molecular mechanism underlying the classical form of. *Am. J. Hum. Genet.* 66, 1766–1776.
- Wenstrup, R.J., Florer, J.B., Brunskill, E.W., Bell, S.M., Chervoneva, I., and Birk, D.E. (2004). Type V collagen controls the initiation of collagen fibril assembly. *J. Biol. Chem.* 279, 53331–53337.
- Xiao, F., Wen, X., Tan, X.H.M., and Chiou, P.-Y. (2018). Plasmonic micropillars for precision cell force measurement across a large field-of-view. *Appl. Phys. Lett.* 112, 033701.
- Zangle, T.A., Burnes, D., Mathis, C., Witte, O.N., and Teitell, M.A. (2013a). Quantifying biomass changes of single CD8+ T cells during antigen specific cytotoxicity. *PLoS ONE* 8, e68916.
- Zangle, T.A., Chun, J., Zhang, J., Reed, J., and Teitell, M.A. (2013b). Quantification of biomass and cell motion in human pluripotent stem cell colonies. *Biophys. J.* 105, 593–601.
- Zangle, T.A., Teitell, M.A., and Reed, J. (2014). Live cell interferometry quantifies dynamics of biomass partitioning during cytokinesis. *PLoS ONE* 9, e115726.
- Zheng, B., Zhang, Z., Black, C.M., de Crombrughe, B., and Denton, C.P. (2002). Ligand-dependent genetic recombination in fibroblasts : a potentially powerful technique for investigating gene function in fibrosis. *Am. J. Pathol.* 160, 1609–1617.
- Zoppi, N., Chiarelli, N., Ritelli, M., and Colombi, M. (2018). Multifaced Roles of the  $\alpha\text{v}\beta 3$  Integrin in Ehlers-Danlos and Arterial Tortuosity Syndromes' Dermal Fibroblasts. *Int. J. Mol. Sci.* 19 <https://doi.org/10.3390/ijms19040982>.

STAR★METHODS

KEY RESOURCES TABLE

REAGENT or RESOURCE	SOURCE	IDENTIFIER
<b>Antibodies</b>		
Rabbit anti-Vimentin	Abcam	Cat# ab47003; RRID: AB_2257290
Mouse anti-smooth muscle actin	Dako	Cat# M0851; RRID: AB_2223500
Mouse anti-integrin $\alpha V\beta 3$	Abcam	Cat# ab7166; RRID: AB_305742
Mouse anti-integrin $\alpha V\beta 5$	R&D	Cat# MAB2528; RRID: AB_2280706
Rabbit anti-cardiac troponin I	Abcam	Cat# ab47003; RRID: AB_869982
Rabbit Anti-Mouse Collagen Type I	Cedarlane Laboratories	Cat# CL50151AP; RRID: AB_10061240
Rabbit anti-RFP	Rockland	Cat# 600-402-379; RRID: AB_828391
Rat anti-integrin $\alpha V$ , PE-conjugated	Invitrogen	Cat# 12-0512-82; RRID: AB_465704
Rat anti-integrin $\alpha 5$ , PE-conjugated	BioLegend	Cat# 103805; RRID: AB_313054
Rat anti-integrin $\beta 1$ , PE-conjugated	Invitrogen	Cat# 12-0181-82; RRID: AB_465572
American hamster anti-integrin $\beta 2$ , PE-conjugated	Invitrogen	Cat# 12-0291-82; RRID: AB_763478
Rabbit anti-integrin $\alpha V\beta 3$	ThermoFisher Scientific	Cat# MA5-32195; RRID: AB_2809482
Rabbit anti-integrin $\alpha V\beta 5$	Bioss Antibodies	Cat# bs-1356R; RRID: AB_10853044
Alexa Flour 594 conjugated WGA	Invitrogen	W11262
<b>Chemicals, Peptides, and Recombinant Proteins</b>		
Cilengitide	MCE	HY-16141
Tamoxifen	Sigma	T5648
Human basic fibroblast growth factor	Millipore	GF003
Protease Inhibitor Cocktail	Sigma	P8340
<b>Critical Commercial Assays</b>		
RNAscope Multiplex FL reagent kit v2	ACD bio	323100
Sircol Insoluble Collagen Assay Kit	Biocolor	S2000
RNeasy Mini Kit	QIAGEN	74104
Masson Trichrome Stain Kit	Thermo Fisher Scientific	87019
Pierce Quantitative Colorimetric Peptide Assay	Thermo Fisher Scientific	23275
M.O.M Immunodetection Kit, Basic	Vector	BMK-2202
Avidin/Biotin blocking kit	Vector	SP-2001
Fluorescein avidin DCS	Vector	A-2001
<b>Deposited Data</b>		
HMDP ventricular expression array data	<a href="#">Rau et al., 2017</a>	GSE48760
Myocardial infarction RNaseq data	This paper	GSE151834
Myocardial infarction single cell RNaseq data from wild-type mouse	This paper	GSE152122
Myocardial infarction single cell RNaseq data from Col5a1CKO mouse	This paper	GSE151695
Myocardial infarction single cell RNaseq data from Col5a1CKO mouse treated with cilengitide	This paper	GSE151695
Figures for <a href="#">STAR Methods</a>	This paper	Mendeley Data <a href="https://doi.org/10.17632/z3vsb9yvks.2">https://doi.org/10.17632/z3vsb9yvks.2</a>
<b>Experimental Models: Cell Lines</b>		
Mouse: immortalized Col5a1 fl/fl cardiac fibroblast	This paper	N/A
Mouse: primary cardiac fibroblast	This paper	N/A

(Continued on next page)

**Continued**

REAGENT or RESOURCE	SOURCE	IDENTIFIER
<b>Experimental Models: Organisms/Strains</b>		
Mouse: Col5a1 fl/fl; C57BL/6	<a href="#">Sun et al., 2011</a>	PMID: 22159420
Mouse: Col1a2-CreERT; C57BL/6	<a href="#">Zheng et al., 2002</a>	PMID: 12000713
Mouse: TCF21-MerCreMer; C57BL/6	<a href="#">Acharya et al., 2011</a>	PMID: 21432986
Mouse: R26RtdTomato; C57BL/6	The Jackson Laboratory	007914
Mouse: C57BL/6	The Jackson Laboratory	000664
Mouse: Col5a1 KO; C57BL/6	<a href="#">Wenstrup et al., 2004</a>	PMID: 15383546
<b>Oligonucleotides</b>		
Mouse Col1a1-C1 probe	ACD bio	319371
Mouse Col3a1-C2 probe	ACD bio	455771-C2
Mouse Col5a1-C3 probe	ACD bio	521291-C3
Quantitative real-time PCR Primers	<a href="#">Table S3</a>	N/A
<b>Recombinant DNA</b>		
Ef1a_Large T-antigen_Ires_Puro	<a href="#">Mali et al., 2008</a>	Addgene#18922
Lenti-pHIV-EGFP	<a href="#">Welm et al., 2008</a>	Addgene#21373
psPAX2	Trono Lab Packaging and Envelope Plasmids (unpublished)	Addgene#12260
pMD.G2	Trono Lab Packaging and Envelope Plasmids (unpublished)	Addgene#12259
pLV-EGFP-Cre	<a href="#">Truitt et al., 2016</a>	Addgene#86805
<b>Software and Algorithms</b>		
Vevo LAB	VisualSonics	<a href="https://www.visualsonics.com/product/software/vevo-lab">https://www.visualsonics.com/product/software/vevo-lab</a>
ImageJ	NIH	<a href="https://imagej.nih.gov/ij/">https://imagej.nih.gov/ij/</a>
FolwJo	FolwJo	<a href="https://www.flowjo.com">https://www.flowjo.com</a>
Cellranger mkfastq	10x Genomics	3.0.2
R package Seurat	Bioconductor	3.0.2
Proteome Discoverer	Thermo Fisher Scientific	2.2
WGCNA	CRAN	<a href="https://cran.r-project.org/web/packages/WGCNA/index.html">https://cran.r-project.org/web/packages/WGCNA/index.html</a>
pheatmap	CRAN	<a href="https://cran.r-project.org/web/packages/pheatmap/index.html">https://cran.r-project.org/web/packages/pheatmap/index.html</a>
Prism 8	GraphPad	N/A
JPKSPM Data Processing	Bruker, JPK	N/A
UCSF Chimera	RBVI, UCSF	<a href="http://www.cgl.ucsf.edu/chimera/">http://www.cgl.ucsf.edu/chimera/</a>
<b>Other</b>		
Nikon Eclipse Ti2 confocal microscopy	Nikon	<a href="https://www.microscope.healthcare.nikon.com/products/inverted-microscopes/eclipse-ti2-series">https://www.microscope.healthcare.nikon.com/products/inverted-microscopes/eclipse-ti2-series</a>
Vevo 2100 Imaging System	VisualSonics	<a href="https://www.visualsonics.com/product/imaging-systems/vevo-2100">https://www.visualsonics.com/product/imaging-systems/vevo-2100</a>
Q Exactive Plus Hybrid Quadrupole-Orbitrap Mass Spectrometer	Thermo Fisher Scientific	IQLAAEGAAPFALGMBDK
JEM1200EX transmission electron microscope	JEOL	<a href="https://www.jeolusa.com/PRODUCTS/Transmission-Electron-Microscopes-TEM">https://www.jeolusa.com/PRODUCTS/Transmission-Electron-Microscopes-TEM</a>
TF20 TEM	FEI	<a href="https://www.felmi-zfe.at/instrumentation/tem/fei-tecnai-f20/">https://www.felmi-zfe.at/instrumentation/tem/fei-tecnai-f20/</a>
SHOCONGG-TL AFM Probes	AppNano	SHOCONGG-TL
JPK Nanowizard 4A BioAFM	Bruker, JPK	<a href="https://usa.jpk.com/products/atomic-force-microscopy/nanowizard-ultra-speed-2">https://usa.jpk.com/products/atomic-force-microscopy/nanowizard-ultra-speed-2</a>

## RESOURCE AVAILABILITY

### Lead Contact

Further information and requests for resources and reagents should be directed to and will be fulfilled by the Lead Contact, Arjun Deb ([adeb@mednet.ucla.edu](mailto:adeb@mednet.ucla.edu))

### Materials Availability

This study did not generate new reagents.

### Data and Code Availability

The accession number for the bulk RNA sequencing and single-cell RNA sequencing in this paper are available in NCBI GEO dataset. Myocardial infarction bulk RNaseq data: GSE151834, Myocardial infarction sc RNaseq data: GSE152122, Myocardial infarction sc RNaseq data from Col5a1CKO/Control mouse: GSE151695, Myocardial infarction sc RNaseq data from Col5a1CKO mouse treated with cilengitide or vehicle: GSE151695.

Figures for [STAR Methods](#) are available in Mendeley data (<https://doi.org/10.17632/z3vsb9yvks.2>)

## EXPERIMENTAL MODEL AND SUBJECT DETAILS

### Animal care and use

All animal studies were approved by the Animal Research Committee, University of California, Los Angeles. All animals were maintained at the UCLA vivarium according to the policies instituted by the American Association for Accreditation of Laboratory Animal Care. Sample size was estimated based on published literatures on murine myocardial infarction models ([Hinkel et al., 2015](#); [Ren et al., 2005](#)). Male and female animals aged between 10 and 14 weeks were used in the study. All animals belonged to the C57BL/6 strain, were healthy, immune-free, and drug or test naive and were not involved in other experimental procedures. Littermates were used as controls for all experiments.

### Generation of animals with genetically labeled cardiac fibroblasts and fibroblast specific deletion of Col5a1

Col1a2CreERT (B6 background) and TCF21MerCreMer (B6 background) animals were crossed with the lineage reporter Rosa26tdtomato (B6 background) animals to generate progeny animals as described ([Pillai et al., 2017](#)). Tamoxifen was administered for 10 days prior to ischemic cardiac injury followed by RNA-FISH to determine whether genetically labeled fibroblasts co-expressed the RNA signal. For generation of Col5a1CKO mice, Col1a2CreERT or TCF21MerCreMer mice were crossed with the Col5a1 floxed (B6 background) mice ([Sun et al., 2011](#)) and progeny mice were administered tamoxifen (1 mg IP daily) for 5 days prior to ischemic injury and continued for 7 days following injury. For the experiment on TCF21MerCreMer mice to demonstrate an effect of Cre recombinase on heart function and fibrosis, these mice were administered tamoxifen for 5 days prior to ischemic injury and continued for 7 days following injury as as for generating Col5a1CKO mice. For experiments related to administration of tamoxifen after acute injury, TCF21MerCreMer mice crossed with the Col5a1 floxed mice were administered tamoxifen from 4 days to 14 days post injury. Col5a1(+/-) heterozygous KO (B6 background) mice ([Lincoln et al., 2006](#)) were used for experiments to confirm Col5a1CKO post infarction phenotype.

### Murine models of acute ischemic cardiac injury

All animal studies were approved by the Animal Research Committee, University of California, Los Angeles. Myocardial infarction was performed by ligating the left anterior descending (LAD) coronary artery following open thoracotomy as described ([Pillai et al., 2017](#); [Ubil et al., 2014](#)). Briefly, Mice were anesthetized with ketamine (80 mg/kg)/xylazine (20 mg/kg) by intraperitoneal injection. Respiration was provided by mechanical ventilation with 95% O<sub>2</sub> (tidal volume 0.5 ml, 130 breaths/min). The LAD coronary artery was ligated intramurally 2mm from its origin with a 9-0 proline suture.

For experiments related to use of cilengitide, 20mg/kg of Cilengitide diluted in PBS was administered by intraperitoneal injection every day until harvest and PBS was used as vehicle as a control.

### Echocardiogram

Animals was assessed at pretreatment baseline and at the time point of 3 day, 1 week, 2 weeks, 3 weeks, 4 weeks, and 6 weeks post-Myocardial infarction. Animals were continuously anesthetized with 1.5% isoflurane and 95% O<sub>2</sub>. Vevo2100 imaging system and a 30-mHz scan head (Toronto, Canada) were used to acquire short/long axis B-mode and M-mode images. Long axis B-mode view was used for analyzing peak longitudinal strain rate. All measurements and calculations were conducted using Vevo2100 software.



## METHOD DETAILS

### Antibodies and probes

The following primary antibodies, reagents, or probes were used for immunostaining: rabbit anti-Vimentin (1:100, Abcam, ab45939); mouse anti-smooth muscle actin (1:100, Dako, M0851); anti-cardiac Troponin I (1:100, Abcam, ab47003); mouse anti-integrin  $\alpha$ V $\beta$ 3 (1:50, Abcam, ab7166); mouse integrin  $\alpha$ V $\beta$ 5 (1:20, R&D, MAB2528); Alexa Fluor 594 conjugated WGA (5 $\mu$ g/mL, Invitrogen, W11262). For dual RNA-FISH/immunostaining: rabbit anti-RFP (1:50, Rockland, 600-401-379). For flowcytometry: rabbit anti-integrin  $\alpha$ V $\beta$ 3(CD51/CD61) (1:100, ThermoFisher, MA5-32195); rabbit anti-integrin  $\alpha$ V $\beta$ 5 (1:30, Bioss, bs-1356R); PE-conjugated rat anti-integrin  $\alpha$ V (1:20, Invitrogen, 12-0512-82); PE-conjugated rat anti-integrin  $\beta$ 1 (1:20, Invitrogen, 12-0181-82); PE-conjugated american hamster anti-integrin  $\beta$ 2 (1:20, Invitrogen, 12-0291-82); PE-conjugated rat anti-integrin  $\alpha$ 5 (1:100, BioLegend, 103805); PE-conjugated rat IgG isotype control (same dilution for target antibody, BioLegend, 400508). For RNA-FISH: mouse Col1a1-C1 probe (1:50, ACD, 319371); mouse Col3a1-C2 probe (1:50, ACD, 455771-C2); mouse Col5a1-C3 probe (1:50, ACD, 521291-C3).

### Bulk RNA-seq, single-cell RNA-seq and qPCR

For bulk RNA-seq, the injured and uninjured regions of the heart were harvested at different time points following injury, total RNA extracted using RNeasy Mini kit (QIAGEN) and used to generate RNA-Seq libraries followed by sequencing using Illumina 4000 platform (single-end, 65bp). Reads were aligned to the mouse reference genome (mm10) using STAR aligner (Dobin et al., 2013), and used to quantify normalized expression values (RPKM) for annotated genes (Ensembl v.86). RPKM values were used for principal component analysis (PCA) and gene expression visualizations. Differential expression analysis was performed using edgeR quasi-likelihood pipeline (Robinson et al., 2010). Differential expressed genes (DEGs) were identified at FDR 1% and minimum fold-change value of 4.

For sc- RNA-seq, 1wk post MI hearts were harvested and digested by liberase as described later. After digestion, cells were incubated with 10 $\mu$ M Calcein AM (Abcam, ab141420) and flow sorted to identify live cells followed by library preparation. Library was generated by Chromium Single Cell 3' Library Construction (10x Genomics) and sequenced by Illumina NextSeq 500 Sequencing System. After sequencing, fastq files were generated using Cellranger mkfastq (version 3.0.2). The raw reads were mapped to human reference genome (refdata-cellranger-mm10-3.0.0) using cellranger count. Digital expression matrix was extracted from the filtered\_feature\_bc\_matrix folder outputted by the cell ranger count pipeline. Multiple samples were aggregated by cellranger aggr. To identify different cell types and find signature genes for each cell type, the R package Seurat (version 3.0.2) was used to analyze the digital expression matrix. Cells with less than 500 unique molecular identifiers (UMIs) or less than 100 genes, or greater than 50% mitochondrial expression were removed, resulting in a final dataset of 17,826 cells and 21,447 genes for further analysis. The Seurat function NormalizeData was used to normalize the raw counts. Variable genes were identified using the FindVariableFeatures function. The ScaleData function was used to scale and center expression values in the dataset, the number of unique molecular identifiers (UMI) was regressed against each gene. Principal component analysis (PCA), t-distributed stochastic neighbor embedding (tSNE), and uniform manifold approximation and projection (UMAP) were used to reduce the dimensions of the data, and the first 2 dimensions were used in the plots. The FindClusters function was used to cluster the cells. Marker genes were found using the FindAllMarkers function for each cluster. Cell types were annotated based on the marker genes and their match to canonical markers.

For qPCR, For RNA-seq, the injured and uninjured regions of the heart were harvested at different time points following injury, RNA extracted using RNeasy Mini kit (QIAGEN). cDNAs were generated using iScript cDNA Synthesis Kit (BioRad) and qPCR performed.

### Col5a1 correlation with extracellular matrix pathway accounts for clinical trait association in the HMDP

The data used for analysis, including left ventricle expression arrays and clinical traits can be found using the GEO accession: GSE48760 and within the following studies [5, 6]. Midweight bicorrelation coefficients and corresponding p values were generated from HMDP data using the R package WGGNA. To calculate adjusted regressions using the same approaches and compare directly, residuals from each ECM gene correlated with Col5a1 were extracted from the regression using the base lm() function in R. These residuals were then integrated with original expression values and correlated against indicated traits also using WGCNA to enable direct comparisons. For purposes of comparisons, we also adopted a similar approach by collapsing all ECM genes into eigengenes using WGCNA and correlated with either traits or traits adjusted for Col5a1 expression. Distributions of p values resulting from these analyses were compared using a Student's t test (two-way). Plots for visualization were made using either ggplot2 or pheatmap packages in R.

### Proteomic analysis of scar tissue

Injured and uninjured regions of the mouse heart at Day 7 following injury were dissected and homogenized in lysis buffer (200  $\mu$ L, 12 mM sodium lauroyl sarcosine, 0.5% sodium deoxycholate, 50 mM triethylammonium bicarbonate (TEAB)), Sigma Protease Inhibitor Cocktail (0.89 mg/mL final concentration)), then subjected to bath sonication (10 min, Bioruptor Pico, Diagenode Inc. (Denville, NJ)) and heated (95°C, 5 min). An aliquot of the resulting solution (9  $\mu$ L) was taken for measurement of total protein concentration (bicinchoninic acid assay; Micro BCA Protein Assay Kit, Thermo Fisher Scientific, Waltham, MA, using BSA as a standard). The remaining samples were diluted to 0.5 mg protein/mL with lysis buffer, and an aliquot of each (100  $\mu$ L) was treated with tris(2-carbox-

ethyl) phosphine (10  $\mu$ L, 55 mM in 50 mM TEAB, 30 min, 37°C) followed by treatment with chloroacetamide (10  $\mu$ L, 120 mM in 50 mM TEAB, 30 min, 25°C in the dark). They were then diluted 5-fold with aqueous 50 mM TEAB, and incubated overnight with Sequencing Grade Modified Trypsin (1  $\mu$ g in 10  $\mu$ L of 50 mM TEAB; Promega, Madison, WI) following which an equal volume of ethyl acetate/trifluoroacetic acid (TFA, 100/1, v/v) was added. After vigorous mixing (5 min) and centrifugation (13,000  $\times$  g, 5 min), the supernatants were discarded and the lower phases were dried in a centrifugal vacuum concentrator. The samples were then desalted using a modified version of Rappsilber's protocol (Rappsilber et al., 2007) in which the dried samples were reconstituted in acetonitrile/water/TFA (solvent A, 100  $\mu$ L, 2/98/0.1, v/v/v) and then loaded onto a small portion of a C18-silica disk (3M, Maplewood, MN) placed in a 200  $\mu$ L pipette tip. Prior to sample loading the C18 disk was prepared by sequential treatment with methanol (20  $\mu$ L), acetonitrile/water/TFA (solvent B, 20  $\mu$ L, 80/20/0.1, v/v/v) and finally with solvent A (20  $\mu$ L). After loading the sample, the disc was washed with solvent A (20  $\mu$ L, eluent discarded) and eluted with solvent B (40  $\mu$ L). The collected eluent was dried in a centrifugal vacuum concentrator. The samples were then chemically modified using a TMT10plex Isobaric Label Reagent Set (Thermo Fisher Scientific) as per the manufacturer's protocol. The TMT-labeled peptides were dried and reconstituted in solvent A (50  $\mu$ L), and an aliquot (2  $\mu$ L) was taken for measurement of total peptide concentration (Pierce Quantitative Colorimetric Peptide, Thermo Fisher Scientific). The samples were then pooled according to protein content (10  $\mu$ g of peptide from each sample; 100  $\mu$ g total), and desalted using the modified Rappsilber's protocol described above. The dried multiplexed pooled sample was reconstituted in water/acetonitrile with 10mM ammonium bicarbonate (solvent C, 5 $\mu$ L, 98/2, v/v, pH10) prior to fractionation (2.7  $\mu$ L injection) via high pH reversed-phase chromatography using a 1260 Infinity LC System (Agilent Technologies, Santa Clara, CA) and a ZORBAX 300 Extend-C18 column (Agilent Technologies, 0.3  $\times$  150 mm, 3.5  $\mu$ m) equilibrated in solvent C and eluted (6  $\mu$ L/min) with an increasing concentration of solvent D (acetonitrile/water with 10mM ammonium bicarbonate, 80/20, v/v, pH10: min/% D; 0/0, 5/14, 65/60, 75/0, 95/0). The fractions were eluted into a 96-well plate with 20  $\mu$ L of 5% formic acid (FA) in each well over the course of 68 min. The 96 fractions were then condensed into 12 fractions prior to another desalting again using the modified Rappsilber's protocol described above. The eluants were then dried and reconstituted in water/acetonitrile/FA (solvent E, 10  $\mu$ L, 98/2/0.1, v/v/v), and aliquots (5  $\mu$ L) were injected onto a reverse phase nanobore HPLC column (AcuTech Scientific, C18, 1.8 $\mu$ m particle size, 360  $\mu$ m  $\times$  20 cm, 150  $\mu$ m ID), equilibrated in solvent E and eluted (500 nL/min) with an increasing concentration of solvent F (acetonitrile/water/FA, 98/2/0.1, v/v/v: min/% F; 0/0, 5/3, 18/7, 74/12, 144/24, 153/27, 162/40, 164/80, 174/80, 176/0, 180/0) using an Eksigent NanoLC-2D system (Sciex (Framingham, MA)). The effluent from the column was directed to a nanospray ionization source connected to a hybrid quadrupole-Orbitrap mass spectrometer (Q Exactive Plus, Thermo Fisher Scientific) acquiring mass spectra in a data-dependent mode alternating between a full scan ( $m/z$  350-1700, automated gain control (AGC) target  $3 \times 10^6$ , 50 ms maximum injection time, FWHM resolution 70,000 at  $m/z$  200) and up to 10 MS/MS scans (quadrupole isolation of charge states  $\geq 2$ , isolation width 1.2 Th) with previously optimized fragmentation conditions (normalized collision energy of 32, dynamic exclusion of 30 s, AGC target  $1 \times 10^5$ , 100 ms maximum injection time, FWHM resolution 35,000 at  $m/z$  200). The raw data was analyzed in Proteome Discoverer 2.2, which provided measurements of relative abundance of the identified peptides.

### Histological studies

Hearts were harvested under anesthesia and perfused with PBS followed by fixation in 4% formaldehyde in PBS at 4°C for 24 h, and subsequently subjected to dehydration in sucrose solution. Then the hearts were embedded in Tissue-Tek O.C.T compound (SAKURA, Finetek, USA) and sectioned with 10 $\mu$ m-thickness.

For immunostaining, tissue sections were incubated with pre-chilled acetone at  $-20^\circ\text{C}$  for 10 min, blocked in 10% species-specific normal serum in 1% BSA/PBS for 1 h, and primary antibodies diluted in 1% BSA/PBS at 4°C overnight. Secondary antibodies were diluted in PBS and incubated with the sections for 1 h. Samples were counterstained with DAPI (1  $\mu$ g/mL, Invitrogen, D3571) and mounted with SlowFade Gold Antifade reagent (Invitrogen, S36936). Images were taken using Nikon Eclipse Ti2 confocal microscopy (Nikon, USA) and analyzed in NIS Element AR software (Nikon). For detection of  $\alpha$ smooth muscle actin, integrin  $\alpha$ V $\beta$ 3, and  $\alpha$ V $\beta$ 5, M.O.M immunodetection kit (Vector) was used. Briefly, tissue sections were incubated with pre-chilled acetone at  $-20^\circ\text{C}$  for 10 min, incubated with Avidin/Biotin blocking buffer (Vector) for 15 min, M.O.M blocking buffer for 1 h, and primary antibodies diluted in M.O.M diluent at 4°C overnight. Biotinylated 2nd antibody against mouse (Vector) was diluted in M.O.M diluent (1:250) and incubated with the sections for 10 min. Samples were incubated with diluted fluorescein avidin DCS (1:60) for 5 min. Samples were counterstained with DAPI (1  $\mu$ g/mL, Invitrogen, D3571) and mounted with SlowFade Gold Antifade reagent (Invitrogen, S36936).

For Masson Trichrome staining, sections were stained using Masson Trichrome Stain kit (Thermo Scientific, 87019). Images were taken in heart sections from apex, mid-ventricle, and close to suture and fibrotic area analyzed from apex to mid-ventricle. Scar tissue area was calculated as the fraction of left ventricular surface area occupied by the scar tissue. Severity of fibrosis was classified as sample showed  $> 40\%$  fibrotic area as "severe," 20%–40% as "moderate," or  $< 20\%$  as "mild" for 6wks post MI hearts and  $> 50\%$  fibrotic area as "severe," 30%–50% as "moderate," or  $< 30\%$  as "mild" for 2wks post MI hearts.

### RNA-Fluorescence *in situ* hybridization

RNA-FISH was performed using RNAscope Multiplex Fluorescent reagent kit v2 (ACD Inc, USA) as per manufacturer instructions. Tissue sections were incubated with hydrogen peroxide for 15 min followed by incubation with RNAscope Target Retrieval Reagent at 99°C for 5 min. Then the section was incubated with Protease III reagent at 40°C for 30 min in HybEZ II oven (ACD Inc). After pre-treatment steps, RNAscope probes were hybridized at 40°C for 2 h, AMP1 for 30 min, AMP2 for 30 min, AMP3 for 15 min, channel-

specific HRP reagent for 15 min, diluted TSA Plus fluorophores (PerkinElmer, USA) in RNAscope TSA dilution buffer (1:1000 dilution) for 30 min, HRP-blocker reagent for 15 min. Stained section was counterstained with DAPI solution and mounted in SlowFade Gold Antifade reagent (Invitrogen, S36936).

For dual RNA-FISH and immunostaining, tissue sections were pre-treated, and signals developed as described above. Following RNA-FISH, the sections were blocked with 10% normal goat serum/1% BSA in PBS, incubated with anti-RFP (1:50, Rockland, 600-401-379) or anti-cTnI (1:50, Abcam, ab47003) at 4°C overnight, HRP-conjugated secondary antibodies against rabbit (1:200, Invitrogen, #31470) for 30 min, diluted TSA Plus TMR (1:300, PerkinElmer, FP1169) in RNAscope TSA buffer for 15 min, and counterstained with DAPI.

### Insoluble collagen assay

Insoluble collagen assay was conducted using Sircol Insoluble Collagen Assay Kit (Biocolor, S2000). The injured regions of the heart were harvested at 4 weeks following injury and weighed to determine their wet weight. Tissues were homogenized in 0.1 mg/mL pepsin/0.5 M acetic acid and incubated overnight at 4°C. Lysates were centrifuged at 12K r.p.m for 10 min and supernatants were transferred to new tubes. Tissue residues were incubated with Fragmentation Reagent at 65°C for 2 h with vortex every 30 min during incubation, centrifuged at 12K r.p.m for 10 min, and supernatants were transferred into new tubes. Supernatants were mixed with 1 ml of Sircol Dye Reagent and incubated for 30 min with gentle shaking. Precipitates were collected by centrifuge at 12K r.p.m for 10 min and washed with 750 µl of ice-cold Acid-Salt Wash Reagent. Washed precipitates were dissolved in 500 µl of Alkali Reagent, transferred 200 µl of each sample and collagen standards into a 96-well plate, and measured absorbance at 550 nm using Synergy H1 microplate reader (BioTek).

### Transmission electron microscopy

Samples were fixed in 2% glutaraldehyde in PBS at 4°C for 3 h. Fixed samples were embedded in low-viscosity resin (Agar, UK) as follows: samples were osmicated using 1% OsO<sub>4</sub>; stained with 3% uranyl-acetate; dehydrated in 30-50-70-95%-100% ethanol and embedded in low-viscosity resin (Agar, UK). Plastic-embedded samples were sectioned using UCT ultramicrotome (Leica, Austria) and diamond knife (Diatome, Austria). Sections 50-55 nm thick were mounted on home-made EM grid(s) with plastic-carbon support film, stained with saturated uranyl-acetate and Sato's lead-citrate. Sections were imaged using JEM1200EX transmission electron microscope (JEOL, Japan) at 80 kV equipped with BioScan600W digital camera (Gatan, USA). Images were prepared for publication using a Photoshop (Adobe, USA). Approximately 500 fibrils were measured by ImageJ for analyzing fibril diameter in each group.

### Tomography of collagen fibers

Sections 200 nm thick were mounted on 150 mesh hexagonal copper grids (Ted Pella, USA). Thereafter, grids with attached sections were stained with saturated uranyl acetate, lead citrate, 10 nm gold from both sides. Layer of carbon was evaporated on top of the section. Grids were loaded into high-resolution tomography holder Model 2020 (Fischione, USA) and imaged with TF20 TEM (FEI, Netherlands) at 200 kV. To collect tomograms, FEI Batch Tomography software was used. The tomograms were processed using IMOD software (Kremer et al., 1996). Alignment of the stack was performed using fiducial markers (10 nm gold) on both sides of the tomogram. The final 3D model calculation was performed by SIRT (IMOD). Obtained 3D models were visualized in Chimera (Pettersen et al., 2004). They were filtered with Gaussian filter and segmented in Segger, part of Chimera package. Final models were imaged in Chimera also.

### Plasmid construction and Lentivirus preparation

pLenti-Large T antigen (Cat#18922), Lenti-pHIV-eGFP (Cat#21373), PSPAX2 (Cat#12260), PMD.G2 (Cat#12259), pLV-eGFP-Cre (Cat#86805) were purchased from Addgene. Total 13 µg plasmids (object gene, PSPAX2, PMD.G2) was co-transfected into 75 cm<sup>2</sup> flask with 293T cells in 10 mL DMEM Medium, 6-7 mL fresh DMEM medium were changed after plasmids co-transfected 8-10 h. The medium was collected and centrifuged at 4°C in 500x g for 10 min after transfected 72 h. The medium with virus was aliquoted and stored at -80°C.

### Isolation of primary culture adult cardiac fibroblast

5-7 hearts were harvested from wild-type C57BL/6 mice or Col5a1 floxed mice. Valves and atriums were removed from the hearts, and the hearts rinsed in ice-cold HBSS. The hearts were chopped into 1 mm square pieces, suspended in 0.1 µg/mL liberase TH (Sigma, 5401151001) in Tyrodes buffer (136 mM NaCl, 5.4 mM KCl, 0.33 mM NaH<sub>2</sub>PO<sub>4</sub>, 1 mM MgCl<sub>2</sub>, 10 mM HEPES, 0.18% Glucose), and incubated with shaking incubator at 37°C for 30 min at 80 rpm. Digested hearts were filtered with a 40 µm cell strainer (Fisher, 22363547), centrifuged at 200x g for 5 min, resuspended cells with 10 mL of 20% FBS in F12K medium, and seeded the cells into 100 mm<sup>2</sup> dish. After 2 h, medium was changed to human basic FGF (10 ng/mL, Millipore, GF003) containing 20% FBS in F12K medium. Isolated cardiac fibroblast was used for experiments in 2<sup>nd</sup> or 3<sup>rd</sup> passage.

### Generation of Col5a1 deficient immortalized cardiac fibroblast

Cardiac fibroblasts were isolated from Col5a1 fl/fl mouse as described above. These cells were infected with Lentivirus-Large T antigen in presence of polybrene (8 µg/mL) for 16 h, treated with puromycin (2 µg/mL) for selection of infected cells. Immortalized cells

were cultured with 10%FBS containing high glucose DMEM. Cells so immortalized were then infected with Lentivirus-Cre recombinase or lentivirus-GFP to generate Col5a1 deficient cardiac fibroblast or control cardiac fibroblast, respectively. These cells were cultured for 6-7 days and used for each experiment to determine effects on gene expression. To determine an effect of Cilengitide on these cells, Col5a1<sup>fl/fl</sup> cardiac fibroblasts were pretreated with Cilengitide (1 μM) in 10%FBS containing high glucose DMEM for 1 h before infection with lentivirus-Cre recombinase or lentivirus-GFP. These cells were treated with Cilengitide/vehicle for 7 days and medium was changed every 2 days.

### Flow cytometry

For cultured cardiac fibroblasts, cells were harvested and fixed in 4% formaldehyde/PBS for 10min on ice, incubated for primary antibodies diluted in 1%BSA/PBS for 1 h on ice. For unconjugated antibodies, cells were incubated with diluted Alex Fluor 594 secondary antibody (1:200, Invitrogen). Data was analyzed using Flowjo software.

### Measurement of force generated by Col V deficient cardiac fibroblasts

#### Device fabrication

The device to make microtissues was designed using AutoCAD software (Autodesk Inc., USA). STAR Methods Figure 1A shows the three-dimensional (3D) design of master mold. STAR Methods Figure 1B shows the 3D schematic of the replicated design with wells and two microposts. The top view of the replicated design is shown in STAR Methods Figure 1C. By using a laser cutter with a fine-tuned laser power and speed, poly(methyl methacrylate) (PMMA) master molds were fabricated as shown in STAR Methods Figure 1D. After sticking the mold to a Petri dish with glue, a mixture of polydimethylsiloxane (PDMS) prepolymer and its curing agent with the mass ratio of 20:1 was prepared and poured on the mold. After removing bubbles and curing at 80°C for 2 h, the PDMS was peeled off from the mold as shown in STAR Methods Figure 1E.

#### Fabrication of microtissues

In order to make microtissues, after sterilizing the PDMS platform, a collagen hydrogel at density of 3 mg/mL was prepared. Cardiac fibroblasts were mixed with the gel at density of 5 Million cells/mL. The small well around microposts was filled with the cell-laden gel and then incubated for 1 h to encourage the gel formation. After the incubation, sufficient cell culture media was added to the samples.

#### Measurement of contraction force of microtissues

The pictures of tissues were taken on days 1, 2, and 3 of culture by using ToupView microscope integrated with SeBaView software. The images were then analyzed with ImageJ software to measure the deflection of microposts due to the tissue contraction. The cantilever beam theory was used to quantify tissue force. This theory correlates the tissue force to small deflection of microposts as shown in STAR Methods Figure 1F. The stiffness of microposts can be calculated by Equation 1 and the contraction force can be calculated by Equation 2 by measuring the deflection of the free end of each micropost as follows:

$$k = \frac{3\pi E d^4}{64L^3} \quad \text{Equation 1}$$

$$F = k\delta \quad \text{Equation 2}$$

where  $k$  is the stiffness of each micropost that is a function of length ( $L$ ), diameter ( $d$ ), and Young's modulus of PDMS post ( $E$ ). The Young's modulus of PDMS was considered to be 1.1 MPa (Brown et al., 2005; Wang et al., 2014). In the Equation (2),  $F$  is the contraction force,  $\delta$  is the deflection of free end of the micropost (Beussman et al., 2016; Ma et al., 2019; Oyunbaatar et al., 2016; Ribeiro et al., 2016).

#### Numerical simulation

To confirm the measurements of PDMS deflection and contraction force, finite element analysis (FEA) implemented in COMSOL Multiphysics 5.3 software was used. The FEM model consisted of two cylindrical PDMS microposts with the post height of 3.1 mm and diameter of 0.8 mm inside a well. The microposts were fixed to the well and deemed as a cantilever beam. The PDMS assembly was modeled as linear elastic material with a uniform Young's modulus of 1.1 MPa. After setting appropriate boundary conditions and by applying a single force to the free end of the microposts, the displacement distribution of the microposts were determined as illustrated in STAR Methods Figure 1G. Moreover, the simulation showed a linear relationship between the applied force and micropost deflection, which is in agreement with the cantilever beam theory (STAR Methods Figure 1H).

### Measurement of decorrelation rate of Col V deficient cardiac fibroblasts

Quantitative phase microscopy (QPM) was used to determine decorrelation rate as follows. Cardiac fibroblasts were isolated from Col5a1 floxed mice, immortalized and then treated with a Cre expressing or GFP lentivirus to generate Col5a1CKO or control fibroblasts. Cells were imaged every 5 min for 20 h at 20x with a SID-4 Bio (Phasics) camera to acquire QPM data via quadriwave lateral shearing interferometry (Bon et al., 2009). This was on an Axio-vision Observer Z1 (Zeiss) equipped 0.4 numerical aperture objective lens with illumination was provided by a 660 nm center wavelength collimated LED (Thorlabs). The Col5a1CKO fibroblasts and the



control fibroblasts were imaged with enough spacing between cells to allow for automated particle tracking (Crocker and Grier, 1996; Zangle et al., 2013a) and cell or cell cluster segmentation (Otsu, 1979; Zangle et al., 2013b). Automated detection of cell division events were done by pattern matching (Zangle et al., 2014) of quantitative phase images. Using experimentally determined cell average specific refractive index, quantitative phase shifts is related to the dry biomass of cells (Barer, 1952; Davies and Wilkins, 1952). All image processing was performed using custom MATLAB (MathWorks) scripts.

#### **QPM decorrelation rate via temporal autocorrelation**

We quantified the rate of biomass redistribution by examining the similarity of the QPM data over time through an unbiased estimate of autocorrelation (Bendat and Piersol, 2013) of the phase shift signal. The temporal autocorrelation was normalized with respect to the number of data points used in each autocorrelation window, referenced to the end of the time shift window ( $t_0$ ), and defined as:

$$C_{\phi\phi}(x, y, t_0, \tau) = \frac{w}{(w - \frac{\tau}{\Delta t})} \cdot \frac{\sum_{i=0}^{w-\tau/\Delta t} \phi(x, y, t_0 - i\Delta t) \cdot \phi(x, y, t_0 - i\Delta t - \tau)}{\sum_{i=0}^w [\phi(x, y, t_0 - i\Delta t)]^2}$$

Where  $x$  and  $y$  are the spatial positions after removing rigid translational motion of the cell cluster,  $t_0$  is the time,  $\phi$  is phase shift,  $w$  is the number of images used to calculate the signal, and  $\tau$  is time lag. The autocorrelation was then averaged over the cell or cluster area as:

$$\overline{C_{\phi\phi}(t_0, \tau)} = \frac{1}{A} \sum_{\text{all } x, y \text{ in } A} C_{\phi\phi}(x, y, t_0, \tau)$$

where  $A$  is the area of the cell or cluster in pixels. The slope of a linear least-squares fit to the averaged autocorrelation from  $\tau = 0$  to  $\tau = 1$  h (12 frames) was defined as the decorrelation rate and used to quantify the biomass redistribution rate within cell clusters. Any decorrelation rate measurements that included images with mitotic cells were excluded.

### **Traction force measurement of neonatal rat ventricle myocyte and fibroblast co-culture**

#### **Fabrication of bio-sensor devices**

The bio-sensor devices were fabricated by first spin coating a layer of photoresist (AZ 4620, 2500rpm, 60 s) onto a glass slide, and baking it at 90 Celsius for 3 min. Then, gold nanoparticles suspended in citrate buffer (Sigma-Aldrich 742090) were deposited onto the photoresist and left to dry in a vacuum desiccator (Thermo Scientific 53100250) overnight, as illustrated in STAR Methods Figure 2A. A mixture of polydimethylsiloxane (PDMS) comprising 1 part of Sylgard 184 (Dow Corning) with 6 parts of Sylgard 527 (Dow Corning) was then poured onto the surface of dried gold nanoparticles. The Sylgard mixture was put under vacuum to remove the air bubbles before a coverslip glass was put on top of it, as shown in STAR Methods Figure 2B. The devices were then left to cure in the oven at 60 Celsius for 12 h. Thereafter, the devices were released by immersing them into acetone overnight to dissolve the photoresist. This reveals the final structure shown in STAR Methods Figure 2C.

#### **Cell Seeding and Microscopy**

Matrigel (at concentration of 83 $\mu$ g/mL) was then coated for 12 h on the surface of the PDMS devices. On day 1, neonatal rat ventricular cardiomyocytes (NRVMs) were seeded at 75% confluence on the devices for the mutant group, and at 90% confluence on the devices for the control group. The confluence in the 2 groups was made different in order to account for the fact that each mutant fibroblast occupies 3 times more area than each control fibroblast. On day 2, control and mutant fibroblasts were separately seeded onto their respective devices. On day 3, the cells were stained with Calcein AM (Invitrogen), before they were imaged under dark field and fluorescence microscopy (Zeiss AxioScope A1, EC Epiplan-Neofluar, 20x, N.A. = 0.5). The gold nanoparticles were also imaged under dark field microscopy. The gold nanoparticles moved when the cells were beating, due to the mechanical coupling between the cells and the substrate.

#### **Machine Learning Model**

Before we could process the images obtained from microscopy, the numerical model needed to be built. The numerical model was built by first generating 1000 different random continuous stress distributions in COMSOL (finite element software) by using 2-dimensional random functions. An example of the stress distribution is shown in STAR Methods Figure 2D. The stress distributions were applied as boundary loads onto the top surface of the device in COMSOL. Stationary studies were done in COMSOL to solve for the equilibrium displacement of the PDMS surface. One example of the displacement of the PDMS surface is shown in STAR Methods Figure 2E. Thereafter, the 1000 different cases of stresses and displacements were used to train the linear regression machine learning model (scikit-learn).

#### **Processing of Experimental Images**

An area spanning 200 $\mu$ m by 200 $\mu$ m was selected from the video taken by a 20x magnification objective lens under a dark field microscope (Zeiss AxioScope A1, EC Epiplan-Neofluar, 20x, N.A. = 0.5). Two image frames were used to calculate the displacement of the gold nanoparticles. The reference frame was chosen as the frame in which the cells were not beating. The peak frame was chosen as the frame in which the cells and gold nanoparticles had the largest displacement. The positions of the gold nanoparticles were

determined using the Gaussian fitting method as described (Xiao et al., 2018). The displacement was taken to be the difference in the positions of the gold nanoparticles between the peak frame and the reference frame. STAR Methods Figures 2F and 2G show the displacement of each of the gold nanoparticles. The displacements in STAR Methods Figures 2F and 2G were then interpolated and a two-dimensional Fourier transform filter was applied to process the interpolated data to eliminate the components of high spatial frequencies. The resulting interpolated displacements after Fourier filtering are shown in STAR Methods Figures 2H and 2I. The displacements from STAR Methods Figures 2H and 2I were then input into the machine learning model. The machine learning model then output the stress distributions as shown in STAR Methods Figures 2J and 2K. The predicted stress distributions were then inputted back into the COMSOL software to confirm that the simulated displacements (STAR Methods Figure 2L) match with the interpolated displacements (STAR Methods Figure 2H) with an overall error of 2% for the control group. The overall error of the displacements was 10% for the mutant group (STAR Methods Figures 2I and 2M). The errors were calculated by the expression:

$$\sigma = \frac{\sum_{x,y} (u_{\text{simulated}}(x,y) - u_{\text{actual}}(x,y))^2 + \sum_{x,y} (v_{\text{simulated}}(x,y) - v_{\text{actual}}(x,y))^2}{\sum_{x,y} (u_{\text{actual}}(x,y))^2 + \sum_{x,y} (v_{\text{actual}}(x,y))^2}$$

where  $u_{\text{simulated}}(x,y)$  and  $v_{\text{simulated}}(x,y)$  are the x and y vector components of the simulated displacement from COMSOL in STAR Methods Figure 2L, and  $u_{\text{actual}}(x,y)$  and  $v_{\text{actual}}(x,y)$  are the x and y vector components of the displacement in STAR Methods Figure 2H. Note that the displacements are functions over space (x,y). It can be seen that the magnitude of the stresses is larger for the control group STAR Methods Figure 2J as compared to the mutant group STAR Methods Figure 2K.

### Parallel microfiltration

To measure the deformability of wild-type and *Col5a1* null fibroblasts, we used parallel microfiltration (PMF) as described in our previous studies (Kim et al., 2016; Kim et al., 2019; Qi et al., 2015) to assess the ability of cells in a suspended state to filter through 10  $\mu\text{m}$  pores of a membrane in response to applied pressure. The volume of retained cell suspension retained in the top well indicates the number of pores that are occluded, which is largely determined by cell deformability: lower retention indicates a sample with more deformable cells. Polycarbonate membranes with 10  $\mu\text{m}$  pore size (TCTP14250, Millipore) were used for all filtration experiments. Prior to the PMF assay, trypsinized cells were rested 20 m at room temperature, counted using an automated cell counter (TC20, Bio-Rad), and resuspended in medium to a density of  $5 \times 10^5$  cells/mL. Cell suspensions (400  $\mu\text{L}$ ) were loaded into each well of a 96-well plate sample loading plate (4 wells per sample). We measured cell viability by staining cells with Trypan Blue (T8154, Sigma) and verified that cell suspensions prior to filtration consisted of single cells; therefore, the filtration behavior is largely determined by the occlusion of viable single cells rather than apoptotic cells or larger aggregates of cells. Since cell size can also impact occlusion, we measured cell size distributions and confirmed there were no significant size differences between wild-type and knock-out cells in a suspended state (Figure S7A). To drive cell suspensions to filter through the 10  $\mu\text{m}$  pores, we applied an air pressure of 2.0 kPa for 30 s. To quantify retention volume, we transferred the cell suspension retained in the top well after filtration to a 96-well plate and measured the absorbance of phenol red at 562 nm using a plate reader (SpectraMax M2, Molecular Devices). Using a standard curve, we calculated the retained volume. Retention was determined by the volume of cell suspension that remains in the top well after filtration divided by the initial volume loaded ( $\text{Volume}_{\text{final}}/\text{Volume}_{\text{initial}}$ ).

### Atomic force microscopy

For atomic force microscopy (AFM) experiments, PBS-perfused hearts were dissected and mounted in OCT (Tissue-Tek, Sakura Finetek, Torrance, CA, USA) and flash frozen in liquid nitrogen-cooled isopentane. Cardiac tissue cryosections (30  $\mu\text{m}$ ) were mounted onto microscope slides with an adhesive coating (#SUMGP14 Matsunami Glass Ind. Ltd., Kishiwada, Osaka, Japan). Cardiac sections were incubated in rabbit anti-mouse collagen type I antibody (CL50151AP-1; 1:250; Cedarlane Labs) in PBS at 4°C overnight and were detected by indirect immunofluorescence using Alexa Fluor 488 goat anti-rabbit secondary antibody (AB150156; 1:500; Abcam). AFM measurements were performed on each section in PBS using a JPK Nanowizard 4A BioAFM with a 200x200x200  $\mu\text{m}$  HybridStage (Bruker/JPK BioAFM, Billerica, MA, USA) coupled to a Leica M205 stereoscope (Leica Microsystems, Wetzlar, Germany). Scar regions were identified by collagen I dense immunofluorescence signal which was used as a guide for overlaying the AFM cantilever for force spectroscopy (Figures 6B and 6C). Non-scar regions were selected in areas where collagen I signal was confined to the interstitial matrix surrounding cardiomyocytes and at least 1000  $\mu\text{m}$  away from a scar region. Both scar regions and non-scar regions were probed with AppNano SHOCONGG-TL cantilevers with a 10  $\mu\text{m}$  silicon dioxide sphere (nominal freq (kHz) = 21(8-38),  $k(\text{N/m}) = 0.14$  (0.01-0.6); AppNano, Mountain View, CA, USA). The sensitivity and spring constant of each probe were calibrated before each experiment using the contact-free calibration method. All measurements were taken in force spectroscopy mode and force-versus-indentation curves were generated from an average of 200 points/sample. Approach and retraction speeds for all force measurements were 2  $\mu\text{m}/\text{sec}$  with a setpoint force of 2.5 nN and a retraction distance of 10  $\mu\text{m}$ . Data analysis was performed using JPKSPM Data Processing software. To evaluate tissue stiffness, Young's modulus was calculated from > 100 AFM force curves, using the Hertz-Sneddon model (Sneddon, 1965). Young's modulus data were plotted and statistics calculated in GraphPad (Prism) software using the Kolmogorov-Smirnov nonparametric test.



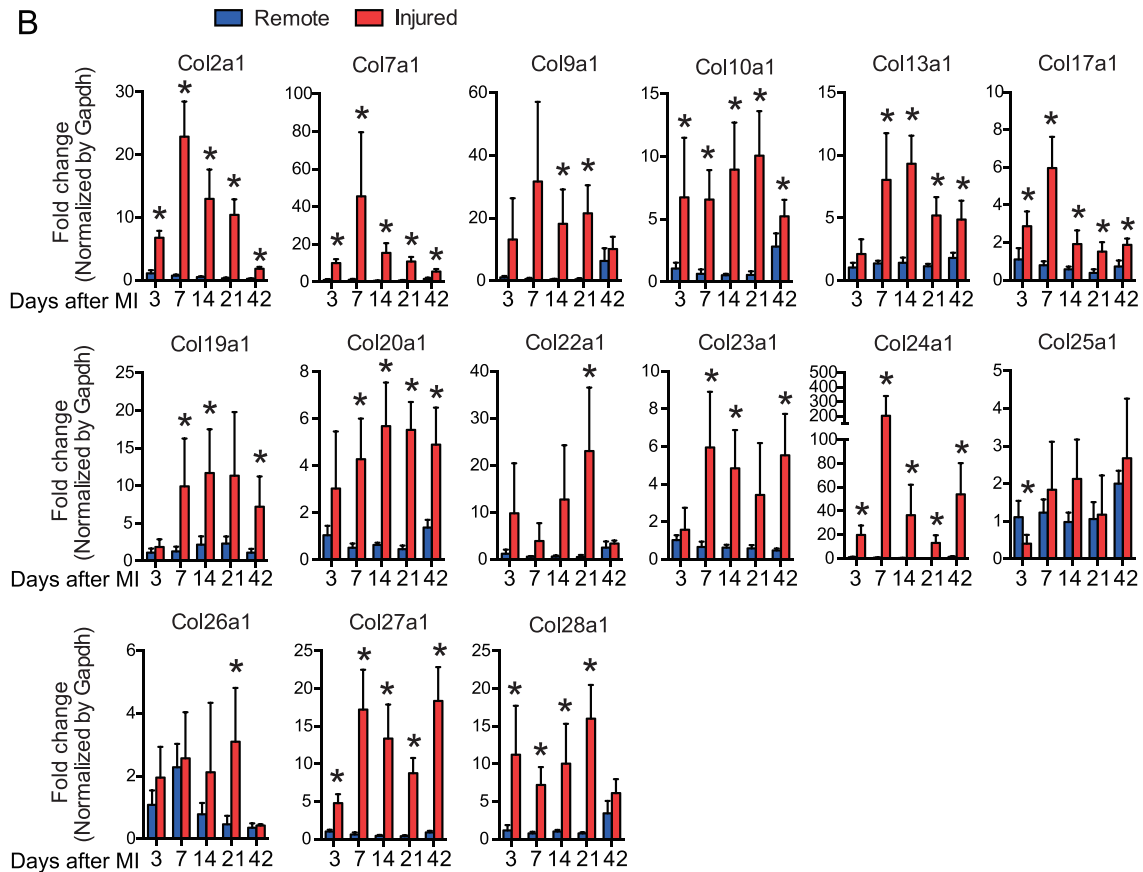
### QUANTIFICATION AND STATISTICAL ANALYSIS

All data is presented as mean  $\pm$  standard deviation (SD) except [Figure 6D](#) (mean  $\pm$  SEM) and mentioned in the figure legends. The exact value of  $n$  is mentioned in the figure legends and always stands for separate biological replicates. Statistical analysis was performed using GraphPad (Prism) software using Student's  $t$  test (Two tailed) and one-way ANOVA with Tukey's multiple comparison analysis as appropriate. A  $P$  value  $< 0.05$  was considered as statistically significant. For analysis of strain imaging data, outlier identification was conducted in ROUT ( $Q = 2\%$ ) method using GraphPad (Prism) software. The values identified as outlier were excluded from statistical analysis.

A

	Basal	3D	7D	14D	21D	42D
EF (%)	65.2±4.6	36.9±11.6	37.3±16.6	33.6±12.2	27.2±10.0	24.3±11.9
FS (%)	35.4±3.5	17.8±6.1	18.3±8.9	16.2±6.3	12.8±4.9	11.4±5.8

B



C

0	0	0	0	0	0	6	3	3	1	Col2a1
0	0	0	0	0	5	4	5	5	4	Col27a1
0	1	0	0	0	0	5	3	2	2	Col9a2
1	3	3	3	2	0	1	5	5	4	Col4a4
1	2	2	2	2	0	1	4	4	4	Col4a3
0	0	0	0	0	1	3	1	1	1	Col24a1
0	0	0	0	0	1	2	3	3	2	Col4a6
0	0	0	0	0	1	3	1	1	0	Col7a1
2	1	1	1	1	0	1	1	1	1	Col6a6
0	1	1	1	1	1	1	1	2	2	Col28a1
0	0	0	0	0	0	1	0	0	1	Col6a5
0	0	0	0	0	0	0	1	1	1	Col22a1
Remote D3	Remote D7	Remote D14	Remote D21	Remote D42	Injured D3	Injured D7	Injured D14	Injured D21	Injured D42	

(legend on next page)

**Figure S1. Dynamic Changes in Expression of Collagen Genes following Injury, Related to Figure 1**

(A) Temporal changes in ejection fraction (EF) and fractional shortening (FS) after ischemic cardiac injury (data shown as mean  $\pm$  S.D., n = 8 animals/group/time point) (B) qPCR demonstrating temporal changes in collagen genes that are not abundantly expressed in the heart (data shown as mean  $\pm$  S.D., n = 5 animals/group/time point, \*p < 0.05, compared to expression of respective collagen gene in uninjured region at that time point) (C) Heatmap demonstrating temporal changes in collagen genes (that are usually expressed in extra cardiac tissues) as well as RPKM values from RNA-seq of injured and uninjured region of heart demonstrating low expression of such collagen genes.

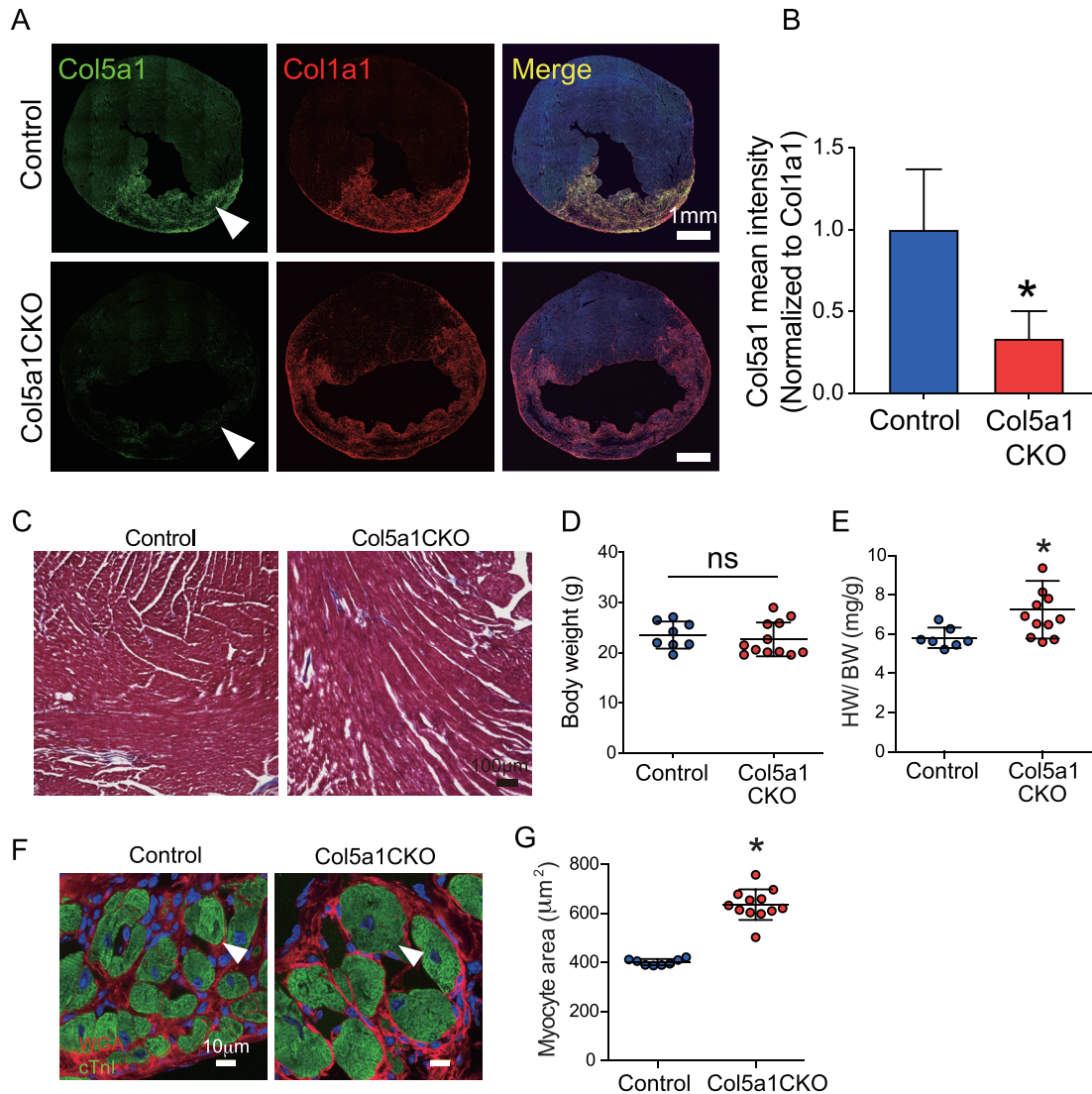


**Figure S2. Col5a1CKO Animals Exhibit Decreased Col5a1 Expression and Have Myocardial Hypertrophy after Ischemic Cardiac Injury, Related to Figure 3**

(A) Conditional deletion of Col5a1 (Col5a1CKO mice) was performed by crossing mice harboring the Col1a2CreERT driver with Col5a1 floxed mice. RNA-FISH demonstrating decreased expression of Col5a1 in Col5a1CKO mice compared to control littermates at 7 days following injury (arrows, representative images, images were acquired and stitched together with Nikon software). The decrease in intensity is compared to Col1a1 in Col5a1 CKO and control littermates. (B) mean intensity of Col5a1 expression normalized to Col1a1 expression in the Col5a1CKO and control animals (mean  $\pm$  S.D., \* $p < 0.05$ ,  $n = 9$  Control and 15 CKO) (C) Masson trichrome staining in remote area of Col5a1CKO and Control animals at 6wks post MI demonstrates minimal fibrosis in both groups. (D) Body weight and (E) Heart weight body weight ratio of Col5a1CKO and control animals at 6 weeks post injury (mean  $\pm$  S.D., \* $p < 0.05$ ,  $n = 8$  control and 12/CKO, ns: not significant). (F) Immunostaining for cardiac troponin I and wheat germ agglutinin (WGA) demonstrates increased myocyte surface area in Col5a1CKO animals at 6 weeks following injury (arrows, representative images, same number of animals as above) (G) Quantitation of myocyte surface area in border zone region of Col5a1CKO and Control animals (mean  $\pm$  S.D., \* $p < 0.05$ ,  $n = 8$  control and 12/CKO).

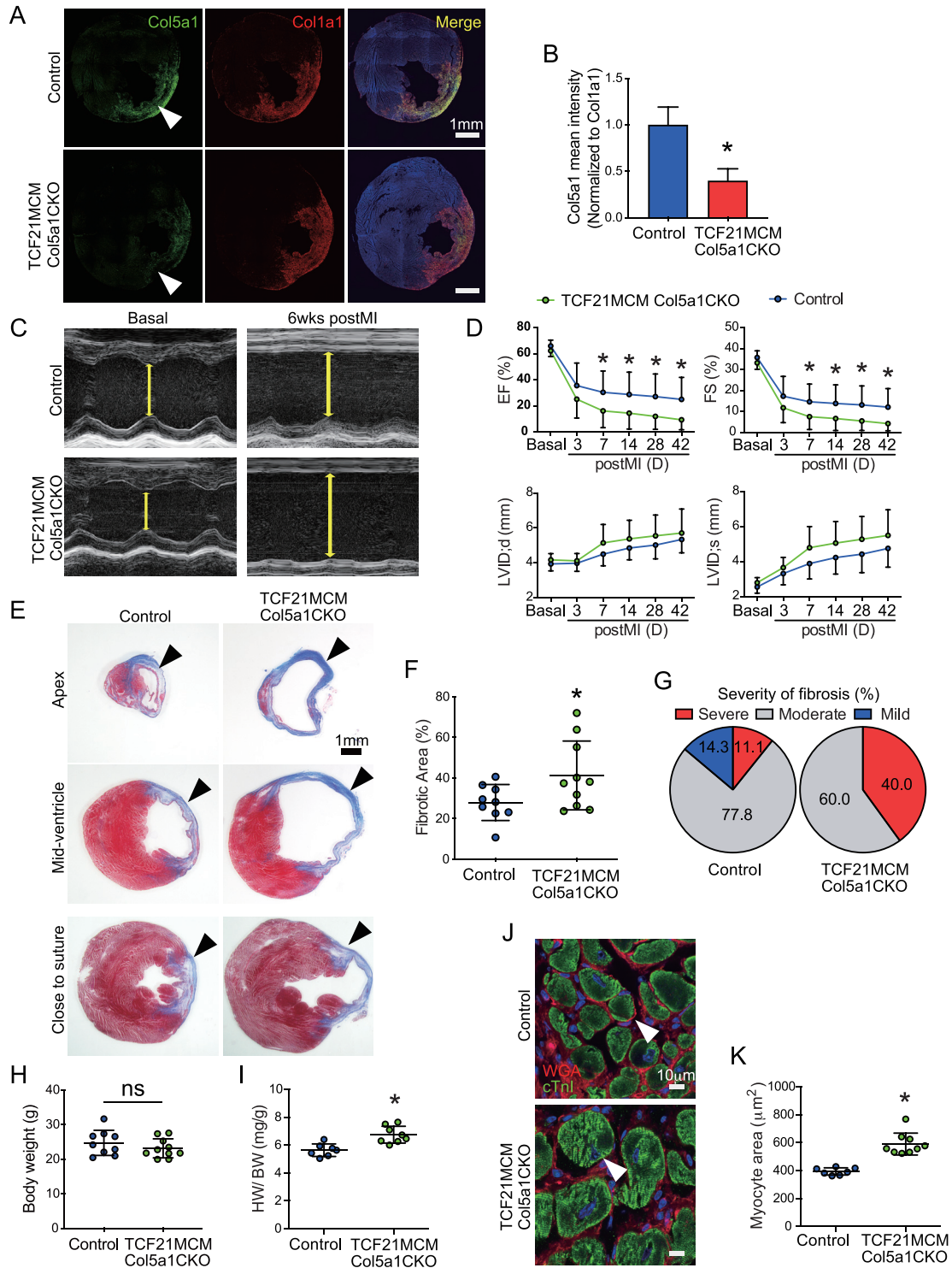


**Figure S3. Col5a1CKO Mice Generated by Using the TCF21MerCreMer Driver Also Exhibit Increased Scarring following Ischemic Heart Injury, Related to Figure 3**

(A) TCF21MCM:Col5a1CKO mice were generated by crossing the TCF21MerCreMer mice with the Col5a1 floxed mice. Expression of Col5a1 in the injury region by RNA-FISH in TCF21MCM:Col5a1CKO animals compared to control littermates at 7 days post MI (arrows, representative images, images were acquired and stitched together with Nikon software). (B) Quantitative decrease in Col5a1 expression in TCF21MCM:Col5a1CKO mice compared to control littermates (mean  $\pm$  SD., \*p < 0.05, n = 6 animals/Control and 4/CKO). (C) M mode echocardiogram demonstrating left ventricular walls and internal dimension (yellow line) prior to (basal) and 6 weeks following injury in TCF21MCM:Col5a1CKO and control littermates (representative images, n = 12 Control and 18 CKO at basal. n = 9 Control (legend continued on next page)



---

and 10 CKO at 6wks post MI). (D) Ejection fraction and Fractional shortening in TCF21MCM:Col5a1CKO and control littermates at different time points following injury (mean  $\pm$  S.D., \* $p < 0.05$ ,  $n = 12$  animals/Control and 18/CKO at basal,  $n = 9$ /Control and 14/CKO at 3D post MI.  $n = 9$ /Control and 12/CKO at 1wk postMI,  $n = 9$ /Control and 10/CKO at 2-6wks post MI). Left ventricular dimensions in end diastole (LVIDd) and end systole (LVIDs) at different time points following injury (E) Masson trichrome staining of hearts of TCF21MCM:Col5a1CKO and control littermates sectioned at the base (just distal to suture line) at mid ventricle and apex 6 weeks following injury (representative images shown,  $n = 9$  animals/Control and 10/CKO) (F) Quantification of surface area of scar normalized to the surface area of the left ventricle (mean  $\pm$  S.D., \* $p < 0.05$ ,  $n = 9$  animals/Control and 10/CKO). (G) Fraction of animals in the TCF21MCM:Col5a1CKO and control groups that demonstrate mild/moderate or severe scarring at 6 weeks following injury. (mild scarring  $< 20\%$  of surface area, moderate between 20 and 40% of ventricular surface area and severe  $> 40\%$  of surface area). (H) Body weight in TCF21MCM:Col5a1CKO and control animals at 6 weeks following injury. (mean  $\pm$  S.D.,  $n = 9$  Control and 8 CKO) (I) Heart weight/body weight ratio in TCF21MCM:Col5a1CKO and control animals at 6 weeks following injury. (mean  $\pm$  S.D., \* $p < 0.05$ ,  $n = 9$  Control and 8 CKO) (J) Immunostaining of mid ventricular heart sections of TCF21MCM:Col5a1CKO and control littermates with Troponin I and Wheat germ agglutinin (WGA) at 6 weeks following injury to determine surface area (cross sectional area, arrowhead) of cardiomyocytes (representative images,  $n = 7$  animals/Control and 9/CKO) (K) Quantitation of surface area of individual cardiomyocytes between TCF21MCM:Col5a1CKO and Control groups at 6 weeks following injury (mean  $\pm$  S.D., \* $p < 0.05$ ,  $n = 7$  animals/Control and 9/CKO).

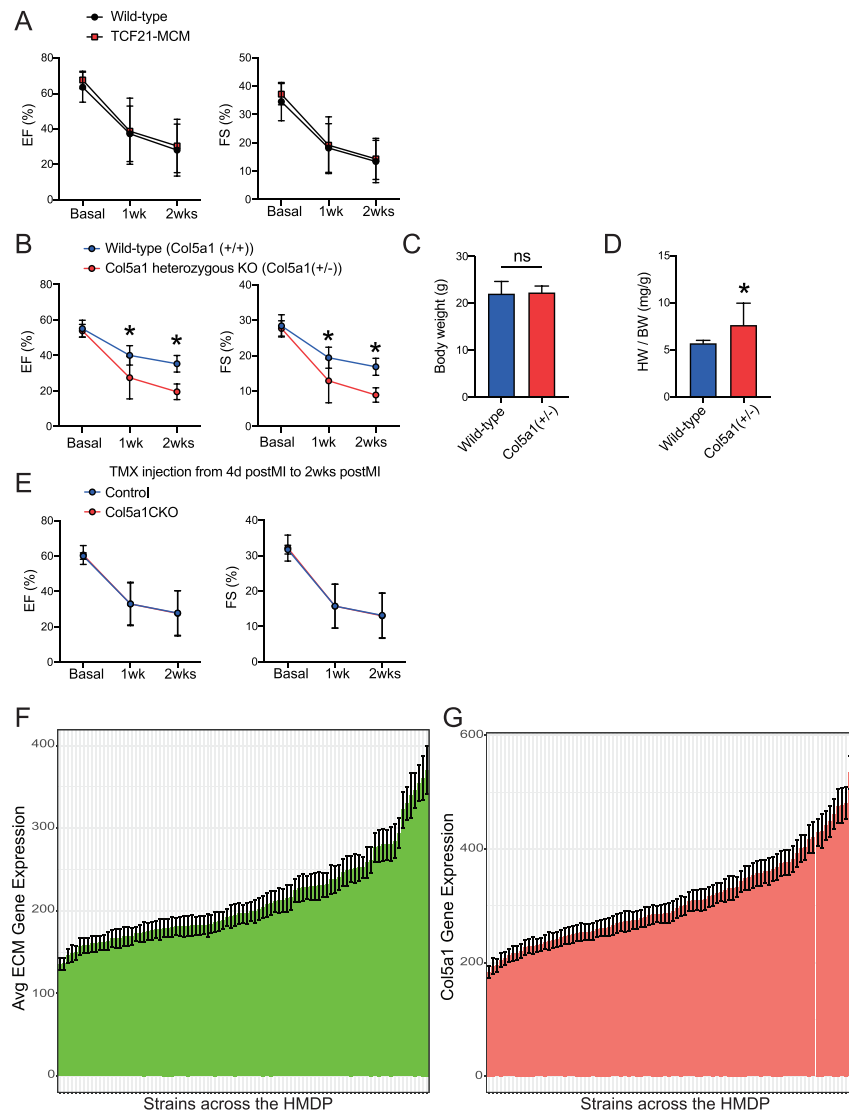


**Figure S4. Cardiac Function and Scarring in TCF21MCM, Col5a1 Heterozygous KO, and TCF21MCM:Col5a1CKO Animals, But with Tamoxifen Administered from Day 4 Onward, and Expression of ECM Genes and Col5a1 across All Strains in the HMDP following Isoproterenol Infusion for 3 weeks, Related to Figures 3 and 4**

(A) TCF21MCM animals and wild type animals were administered tamoxifen and subjected to ischemic cardiac injury. Cardiac contractile function in TCF21MCM and wild type littermates 1 and 2 weeks following injury ( $p > 0.05$ ) ( $n = 4$  for each group)

(B–D) Col5a1 heterozygous KO mice or wild type littermates were subjected to cardiac injury and (B) cardiac function (EF,FS) determined at 1 and 2 weeks after injury ( $*p < 0.05$ ,  $n = 8$  wild-type  $n = 6$  Col5a1 heterozygous KO animals at basal,  $n = 7$  wild-type  $n = 4$  Col5a1 heterozygous KO animals at 1 and 2 weeks after injury) and (C and D) Cardiac hypertrophy assessed by heart weight/body weight ratios ( $*p < 0.05$ ,  $n = 7$  wild-type  $n = 4$  Col5a1 heterozygous animals, ns: not significant) (E) TCF21MCM:Col5a1CKO or control littermates were subjected to ischemic injury but tamoxifen administered for 10 days starting at 4 days after injury. Cardiac contractile function between groups at 1 and 2 weeks after injury ( $n = 8$  control  $n = 7$  Col5a1CKO animals at basal,  $n = 6$  control  $n = 6$  TCF21MCM:Col5a1CKO animals at 1 and 2 weeks after injury,  $p > 0.05$ ).

Average expression of ECM and Col5a1 genes (y axis) versus approximately 96 strains of mice on the x axis. Each data point refers to the average gene expression for ECM genes (F) or Col5a1 (G) in the left ventricle of that particular strain following isoproterenol infusion.

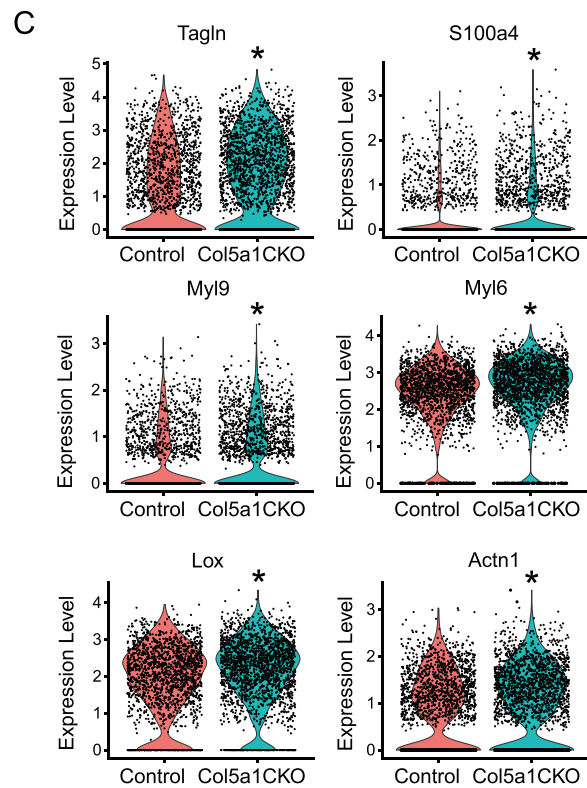
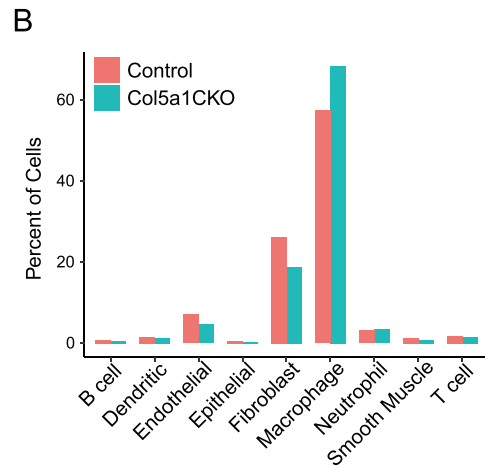
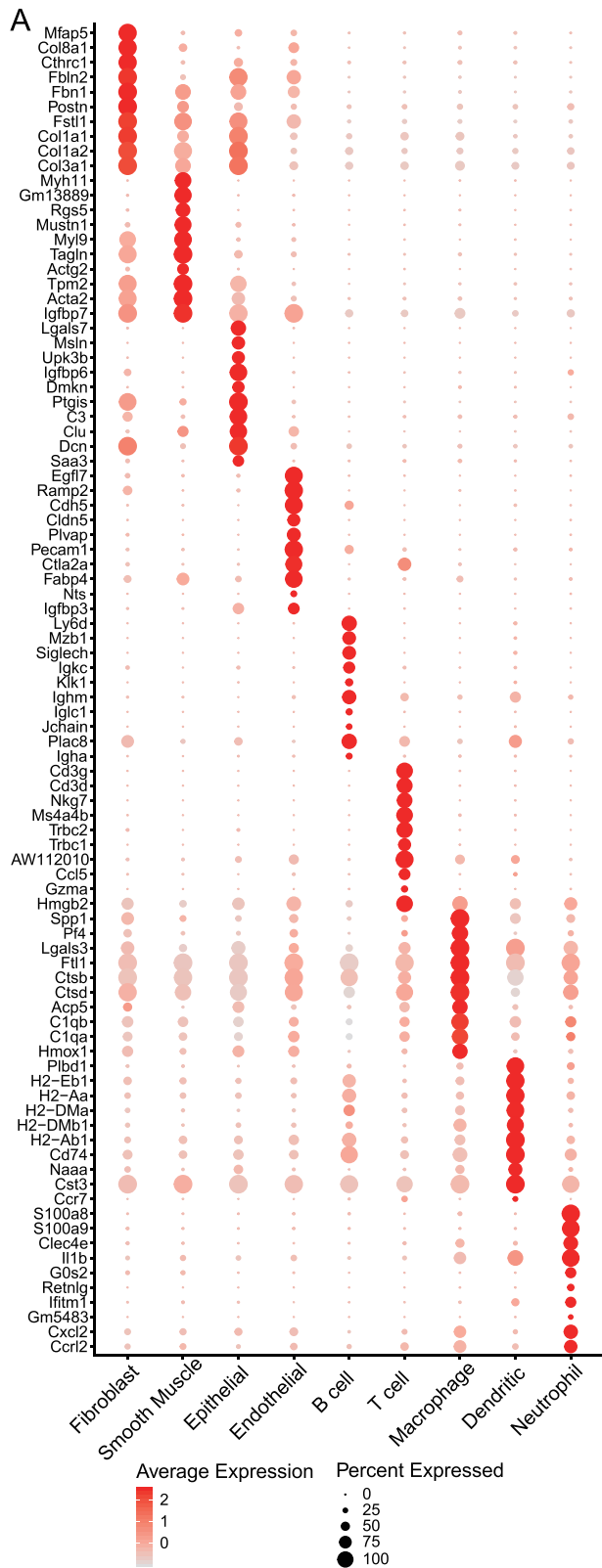
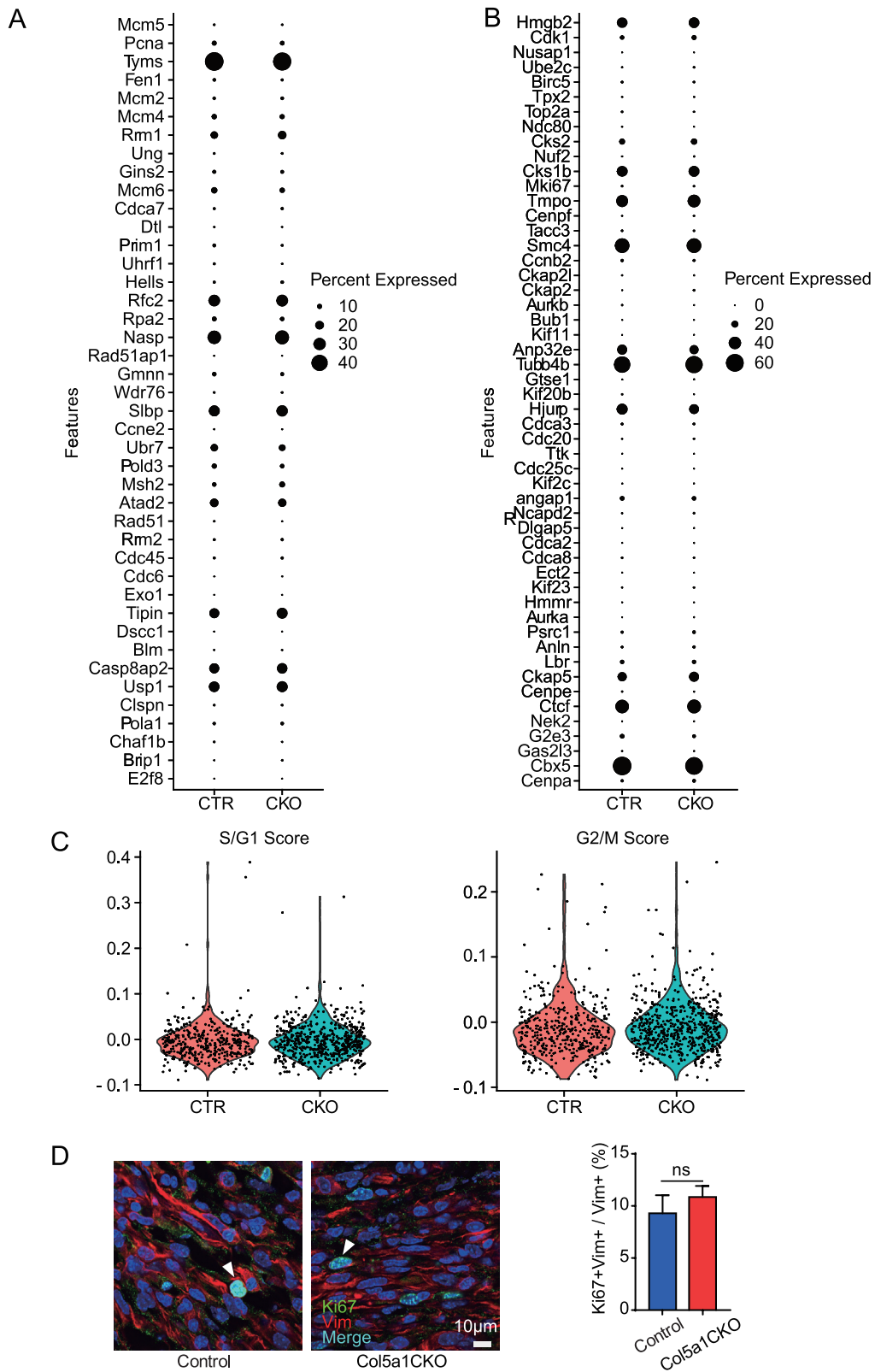


**Figure S5. Identification of Cell Phenotypes According to Expression of Canonical Genes and Numbers of Cells in Each Phenotype in Col5a1CKO and Control Animals from scRNA-Seq Analysis Performed on Non-myocytes at Day 7 following Injury, and Expression of Myofibroblast Genes in Control and Col5a1CKO Cardiac Fibroblasts from Analysis of scRNA-Seq data, Related to Figure 5**

(A) Illustration of clusters of canonical genes used to identify various cell phenotypes of non-myocytes in the heart at 7 days following injury. (B) Fraction of cells in either Col5a1CKO or control animals belonging to each phenotype. ( $n = 3$  samples/group). (C) Expression of smooth muscle contractile proteins or calcium regulatory proteins in cardiac fibroblasts of Control or Col5a1CKO animals. Single cell RNA-seq data analysis demonstrating expression of *Tagln* ( $p = 1.86E-121$ ), *S100a4* (FSP1,  $p = 7.38E-20$ ), *MyI9* ( $p = 1.72E-129$ ), *MyI6* ( $p = 2.82E-107$ ), *Lox* ( $p = 3.68E-37$ ) and *Actn1* ( $p = 7.11E-45$ ) in cardiac fibroblasts in Col5a1CKO and control hearts harvested at 7 days following injury

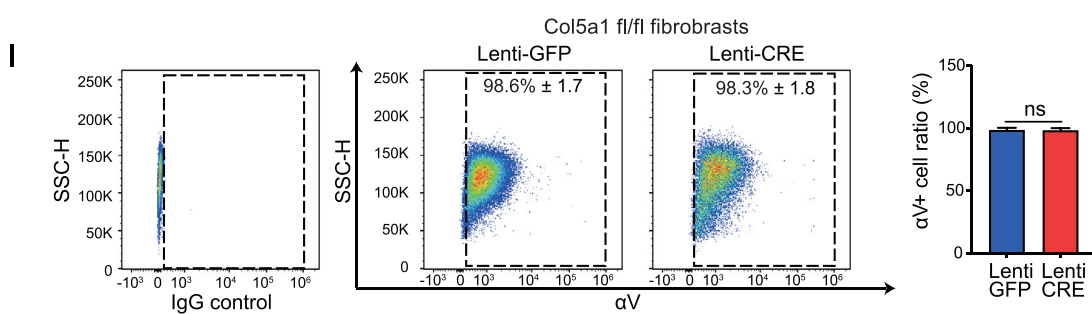
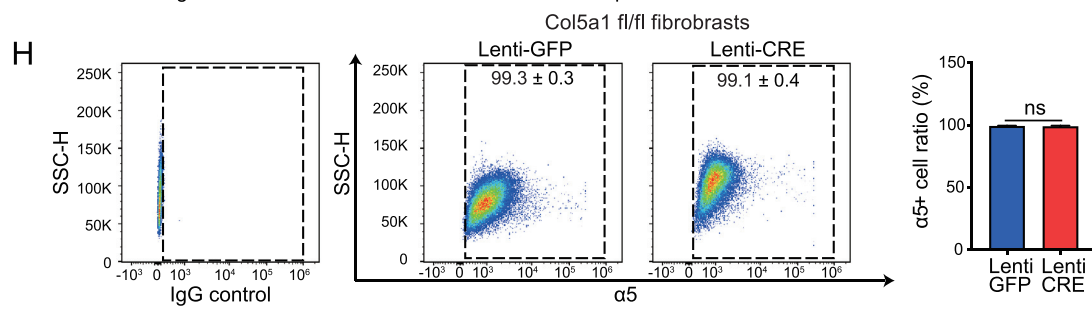
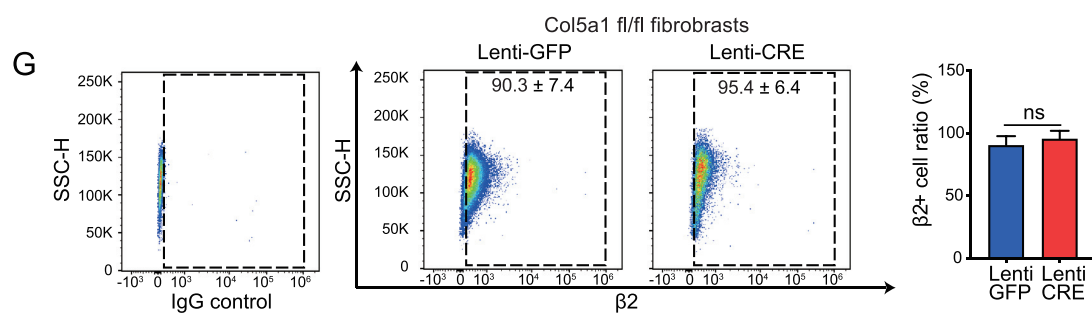
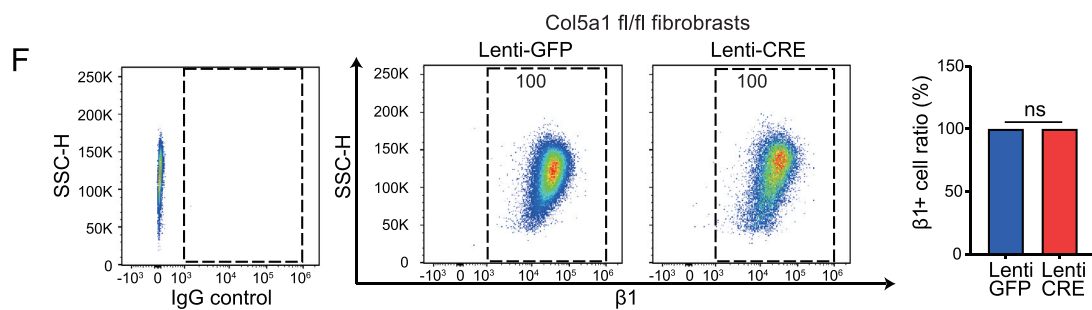
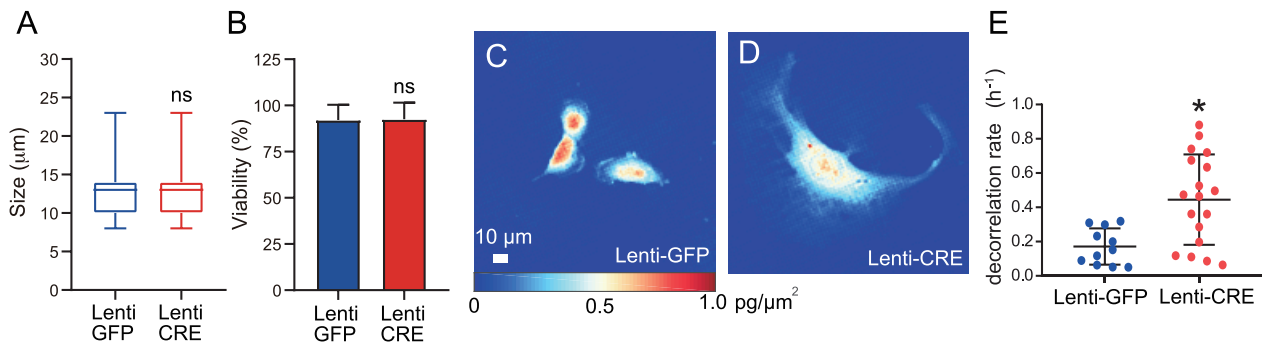




---

**Figure S6. Myofibroblasts in Hearts of Col5a1CKO Animals Do Not Display Higher Rates of Proliferation Compared to That in Control Littermate Animals, Related to Figure 5**

Cluster 0 (myofibroblast population) in both control and Col5a1CKO animals were analyzed for expression of cell cycle genes at 7 days following injury. (A and B) Dot blot demonstrating expression of (A) cell cycle genes regulating S/G1 phase and (B) G2/M phase in both control and CKO animals (C) Violin plot demonstrating average expression of genes regulating S/G1 and G2/M phases in myofibroblasts of Col5a1CKO and control littermates; A score denoting average expression of all cycle genes in S/G1 or G2/M was used and there were no significant differences in expression of genes between the groups. (D) Immunostaining for vimentin and Ki67 (marker of proliferation) in scar tissue of hearts of Col5a1CKO and control animals at 7 days following injury and quantitation of the fraction of proliferating fibroblasts (Ki67+Vimentin+/Vimentin+) (mean  $\pm$  S.D., ns = not significant, representative images shown, n = 6 Control n = 4 CKO)



(legend on next page)

---

**Figure S7. Cell Deformability and Decorrelation Rate of Col5a1CKO and Wild-Type Cardiac Fibroblasts, and Flow Cytometry Demonstrating Expression of Integrins on Col5a1CKO Fibroblasts Generated *Ex Vivo* by Lentiviral Transduction, Related to Figures 6 and 7**

(A) Cell size ( $n > 600$ ) measured right before the PMF assay. Boxplot shows the minimum and maximum with median (line) and whiskers. (B) Cell viability measured by Trypan Blue staining right before the PMF assay. (mean  $\pm$  SD  $n = 3$  independent experiments, ns: not significant). (C-E) Quantitative phase microscopy (QPM) to determine cell stiffness of Col5a1CKO cardiac fibroblasts and control cardiac fibroblasts. (C and D) Representative QPM images demonstrating heatmap of mass/density in (C) control and (D) Col5a1CKO fibroblasts and (E) decorrelation rate of control and Col5a1CKO fibroblasts (mean  $\pm$  S.D.,  $*p < 0.05$ ,  $n = 3$  independent experiments with 11 cell clusters examined/control and 18 cell clusters/Col5a1CKO). Col5a1fl/fl cardiac fibroblasts were infected with Cre or GFP lentivirus and then flow sorted based on GFP expression and then subjected to flow cytometry to determine expression of (F)  $\beta 1$  (G)  $\beta 2$  (H)  $\alpha 5$  (I)  $\alpha V$  integrins (mean  $\pm$  S.D, ns = not significant,  $n = 3$  independent experiments)



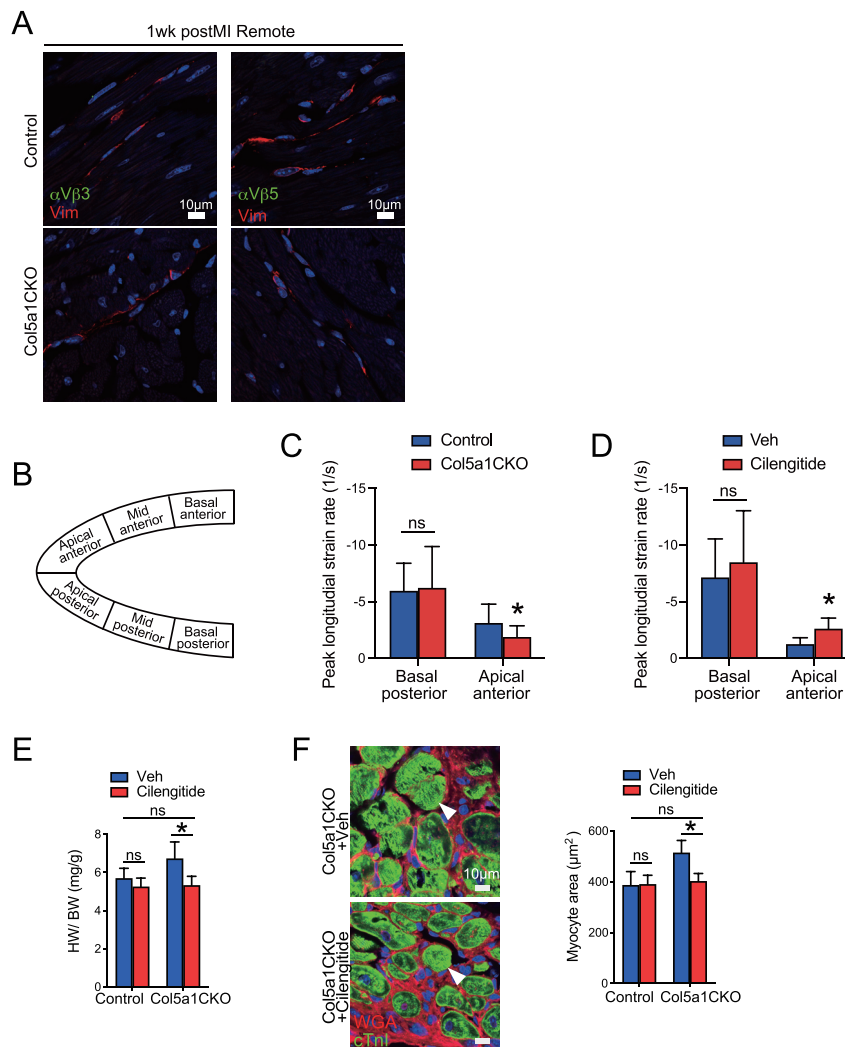


**Figure S8. Effect of Cilengitide on Injured/Uninjured Myocardium and Cardiac Hypertrophy following Ischemic Cardiac Injury, Related to Figure 7**

(A) Immunostaining for vimentin and  $\alpha V\beta 3$  or  $\alpha V\beta 5$  in remote tissue of Col5a1CKO and control littermate heart at 7 days following injury (representative images). (B) A schematic of myocardial regions identified from the parasternal long axis view. (C) Peak longitudinal strain rate of basal posterior and apical anterior region from Col5a1CKO and control littermate at 7 days following injury (mean  $\pm$  S.D., \* $p < 0.05$ , basal posterior;  $n = 18$  animals/Control and 25/CKO apical anterior;  $n = 20$  animals/Control and 22/CKO). (D) Peak longitudinal strain rate of basal posterior and apical anterior region from Col5a1CKO treated with vehicle or cilengitide at 7 days following injury (mean  $\pm$  S.D., \* $p < 0.05$ , basal posterior;  $n = 12$  animals/vehicle and 18/cilengitide. apical anterior;  $n = 10$  animals/vehicle and 18/cilengitide, outliers in the strain imaging data were excluded after identifying them with Prism 8 (ROUT (Q = 2%)). (E) Heart weight/body weight of hearts harvested at 2 weeks following injury (mean  $\pm$  S.D., \* $p < 0.05$ ,  $n = 12$  CKO animals receiving cilengitide,  $n = 6$  CKO animals injected with vehicle,  $n = 9$  control animals receiving cilengitide,  $n = 7$  control animals injected with vehicle) (F) Immunostaining for cardiac troponin and WGA to determine myocyte surface area as a surrogate for hypertrophy in the border zone region of Col5a1CKO animals injected with vehicle or cilengitide (arrows, representative images, mean  $\pm$  S.D., \* $p < 0.05$ ,  $n = 10$ /CKO+Cilengitide,  $n = 6$ /CKO+Veh,  $n = 6$ /animals for all other groups).